Discontinuous precipitation in a nickel-free high nitrogen austenitic stainless steel on solution nitriding

Mohammadzadeh, Roghayeh; Akbari, Alireza; Grumsen, Flemming Bjerg; Somers, Marcel A. J.

Published in:
Philosophical Magazine

Link to article, DOI:
10.1080/14786435.2017.1354135

Publication date:
2017

Document Version
Peer reviewed version

Discontinuous precipitation in a nickel-free high nitrogen austenitic stainless steel on solution nitriding

Abstract

Chromium-rich nitride precipitates in production of nickel free austenitic stainless steel plates via pressurized solution nitriding of Fe-22.7Cr-2.4Mo ferritic stainless steel at 1473K (1200°C) under a nitrogen gas atmosphere was investigated. The microstructure, chemical and phase composition, morphology and crystallographic orientation between the resulted austenite and precipitates were investigated using optical microscopy (OM), X-Ray Diffraction (XRD), Scanning (SEM) and Transmission Electron Microscopy (TEM) and Electron Back Scatter Diffraction (EBSD). On prolonged nitriding, Chromium-rich nitride precipitates were formed firstly close to the surface and later throughout the sample with austenitic structure. Chromium-rich nitride precipitates with a rod or strip-like morphology developed by a discontinuous cellular precipitation mechanism. STEM-EDS analysis demonstrated partitioning of metallic elements between austenite and nitrides, with chromium contents of about 80 wt. % in the precipitates. XRD analysis indicated that the Chromium-rich nitride precipitates are hexagonal $(Cr,Mo)_2N$. Based on the TEM studies, $(Cr, Mo)_2N$ precipitates presented a $(111)_\gamma // (002)_{(Cr.Mo)2N}$, $[1\bar{1}0]_\gamma // [1\bar{1}0]_{(Cr,Mo)2N}$ orientation relationship with respect to the austenite matrix. EBSD studies revealed that the austenite in the regions that have transformed into austenite and $(Cr,Mo)_2N$ have no orientation relation to the untransformed austenite.

Keywords: Discontinuous precipitation; Solution nitriding; Nickel free austenitic stainless steel; EBSD; TEM

1. Introduction

Recently, high nitrogen austenitic stainless steels (HNASSs); especially nickel-free ones (Ni-free-HNASSs), have become of particular interest for the application as biomaterials [1-3]. In the Ni-free-HNASSs the nickel has been substituted with nitrogen as a strong austenite stabilizer [4], thus avoiding the risk for nickel allergy, as well as saving expensive nickel [5-7].

Among the available routes for production of HNASSs, the solid state solution nitriding developed by Berns et al. [8-11] offer two important advantages over the ingot metallurgy carried out in the liquid state under high nitrogen partial pressure [12, 13]; (i) the manufacturing process is not expensive and doesn't involve complex devices compared to casting methods; (ii) the content of nitrogen that can be dissolved in austenite by solution nitriding is higher than what can be achieved via the liquid state [14]. Accordingly, thin plates or wires of nickel free austenitic stainless steels (up to a few millimetres) can be fabricated through solution nitriding of ferritic stainless steel in nitrogen gas within the temperature range of1273-1473K (1000-1200°C).

Cost effective HNASSs offer considerable improvements in mechanical properties over the conventional austenitic stainless steels when they are prepared as single phase microstructure. However, nitrogen saturated meta-stable Fe-Cr alloys are susceptible to undergo chromium nitride precipitation via ordinary or discontinuous solid state reactions during the manufacturing process at relatively high temperatures. This could be take place during isothermal aging as well as during nitriding process. Chromium nitride precipitation during aging of HNASSs has been studied extensively [15-18] and is beyond the scope of the present work.

Studies have shown that [19-24] upon gas or plasma nitriding of Fe-Cr alloys, initially cubic NaCl type CrN nitrides form as coherent or semi-coherent precipitates with a Baker-Nutting (BN) orientation relationship [25]. This initial microstructure, composed of coherent chromium nitrides finely dispersed in the matrix, is commonly referred to as continuously precipitated (CP). Upon nitriding for prolonged time; Fe–Cr alloys with sufficiently high Cr-content undergo a discontinuous cellular precipitation (DCP) reaction [19-24].For example, Hekker et al. [20], Mittemeijer et al. [26] and Wiggen et al. [27]reported the occurrence of lamella-like CrN precipitates with discontinuous mechanism during gas nitriding of Fe-Cr(-C) alloys with 1-4 % Cr. Studies by Schacherl et al. [21] indicated that discontinuous precipitation colonies can also occur in a single crystal sample of Fe-20.3 wt. %Cr (=21.5 at. %) alloy during nitriding at 853K (580°C) at a low nitriding potential of 0.1 $atm^{-1/2}$ for 48 h. Also plasma nitriding of Fe-18 wt. % Cr alloy at 843K (570°C) was reported to lead to discontinuous precipitation [23].

Solution nitriding generally is performed at high temperatures of 1273-1473K (1000-1200°C) enough high to prevent formation of chromium nitrides. Most of the previous studies [28-30] on manufacturing of Ni-free HNASSs by solution nitriding were focused on solution nitriding at nitrogen gas pressure of 0.1 MPa; only very few reports are concerned with solution nitriding under pressurized nitrogen gas conditions [31, 32]. For Fe-24Cr-2Mo-1N nickel free HNASS produced at a nitrogen gas pressure of 0.1 MPa, only formation of single phase austenitic structure has been reported even after long nitriding times of 36h (129.6 ks) [29]. Present authors [32] have observed formation of chromium-rich nitride precipitates during pressurized solution nitriding of Fe-22.7Cr-2.4Mo ferritic stainless steel surprisingly at high process temperature of 1473K (1200°C).

As follows from the calculated phase diagram of Fe-22.7Cr-2.4Mo-N alloy system as discussed in the paper, broadening of the austenite region and enhanced nitrogen solubility can be achieved at enhanced nitrogen gas pressure, giving the impetus for investigating microstructural changes on pressurized solution nitriding of this Fe-Cr-Mo alloy. Such studies seem to be crucial to achieve the desired mechanical and corrosion properties in Ni-free-HNASSs by pressurized solution nitriding. Therefore, this work is intended to investigate the mechanism of chromium-rich nitride precipitation during prolonged pressurized solution nitriding.

2. Experimental Procedure

The Fe-22.7Cr-2.4Mo ferritic stainless steel was prepared by induction melting in an argon atmosphere. The chemical composition after electro slag remelting (ESR) process is given in Table 1. The remelted ingot ($30\times8\times6$ cm^3) was homogenized by annealing at 1100˚C for 48 h and thereafter hot rolled at 1000 ˚C in five passes to a plate of 10 mm thickness. Eventually a plate of 2 mm thickness was obtained by additional four rolling passes. For obtaining recrystallized steel the plates were annealed at 900˚C for one hour. Rectangular specimens of $10\times3\times2$mm^3 were cut from the annealed plates and their surfaces were mechanically polished and cleaned in ethanol before solution nitriding.

Nitrogen was introduced into the steel by high temperature solution nitriding in a horizontal tube furnace. Nitriding was performed at 1200˚C with high purity nitrogen gas (99.9995%) at total pressure of 0.25MPa (=2.5 bar) for 3, 9, 12, 13 and 18 h. The nitrided samples were quenched from 1200˚C into water at the end of the process to prevent austenite decomposition and the formation of nitride precipitates during cooling. In the

following, the samples are designated SN (solution nitrided) followed by the nitriding time, for example sample SN-9H refers to the sample that was solution nitrided for 9h.

Figure 1 represents calculated phase diagram of Fe-22.7Cr-2.4Mo-N alloy system at nitrogen partial pressure of 0.1MPa and 0.25MPa using the Thermo-calc software [33]. Comparing Figure 1 (a) and Figure 1 (b) reveals that pressurized solution nitriding induces broadening of the austenite region and enhances nitrogen solubility. This is besides enhancing nitrogen transport kinetics in the steel.

Microstructural investigations were performed with reflected light microscopy (RLM, Olympus-PMG3), scanning electron microscopy (SEM, JSM-5900 operated at 20 kV) and transmission electron microscopy (TEM, JOEL-JEM-3000I, operated at 300 kV), equipped with spectrometers for energy dispersive X-ray spectroscopy (EDS).For RLM and SEM investigations the samples were prepared by standard metallographic preparation techniques and finally etched in modified aqua regia 50 % HCl-25 % HNO_3-25% H_2O (vol.-%). The thin foil specimens for transmission electron microscopy studies were prepared by mechanical grinding down to 130 µm, followed by twin-jet electrolytic polishing using a Struers-Tenupol 5 apparatus operated at 15.5 V at temperatures ranging of 248-263K (-25 to -10°C), using a solution containing 10% perchloric acid and 10% ethylene glycol monobutyl ether in ethanol.

Electron back scatter diffraction (EBSD) investigations were performed on cross sections of solution nitrided samples using a FEI Helios dual beam FIB-SEM with a field emission gun, an EBSD system from EDAX-TSL and a Hikari camera. Prior to EBSD investigations the cross sections were mechanically polished with an oxide polishing slurry (OPS) as the final stage.

For investigation of the phase composition, X-ray diffraction (XRD) was performed using a Bruker AXS - D8 Discover X-ray diffractometer operated in the Bragg-Brentano configuration applying Cr-K_α radiation (λ=2.2897 Å) and Cu-K_α radiation (λ=1.5406 Å(only for annealed SN-9H sample)). X-Ray diffractograms were recorded with a step size of 0.03°2θ and a counting time of 2 seconds per step in the angular range of 53°-136°2θ.

The average nitrogen content in the un-nitrided and fully nitrided samples was measured using a LECO TN500 nitrogen determinator. In this destructive method the sample's nitrogen content is determined by burning 2 mm thick sample with weight of approximately 1 gram and measuring the thermal conductivity of the resulting nitrogen containing gas in a thermal conductivity (TC) cell. Nitrogen depth profiles were obtained by glow discharge optical emission spectroscopy (GDOES) using a LECO-GDS system.

3. Results and Interpretation

3.1. Nitrogen uptake during solution nitriding

The average absorbed nitrogen contents as a function of the nitriding time are given for selected samples in Figure 2. In general, increasing the nitriding time yielded higher nitrogen content in the samples. An overall non-linear dependence of the nitrogen content on the nitriding time was obtained. During the uptake of nitrogen, ferrite is anticipated to transform into austenite.

As the average nitrogen content in SN-13H and SN-18H sample are about 6.34 and 7.31 at. % (equivalent to 1.67 and 1.94 weight percent, respectively) which are significantly higher than the equilibrium solubility of nitrogen in austenite at 1200°C and 0.25MPa (which is about 1.15 wt. % according to Figure 1) and the uptake of nitrogen does not

appear to approach saturation in Figure 2, other high nitrogen containing phases in addition to austenite are expected to have developed.

The nitrogen concentration depth profiles (in weight percent) for SN-3H, SN-9H and SN-12H samples are shown in Figure 3, along with the untreated steels (base material) for comparison. For the base material (un-nitrided sample), the nitrogen concentration is 0.013 wt. %. The nitrogen concentration increases with solution nitriding to a level of about 1.05 wt. % and 1.12 wt. % for SN-3H and SN-9H samples, respectively. As can be seen from Figure 3, the SN-12H sample exhibits the highest nitrogen concentration of about 2.12 wt. %. Since the nitrided layer thickness (according to Figure 4) in SN-3H, SN-9H and SN-12H samples are greater than 500 micron, it is not possible to get nitrogen depth profile in the investigated samples. Therefore, the GDOES can provide valuable data on the nitrogen content of near surface region in the studied samples.

3.2. X-ray diffractometry

X-ray diffractograms obtained from the surfaces of the base material, SN-3H, SN-9H, SN-12H, SN-13H, SN-18H samples are shown in Figure 4. Actually XRD measurements were performed at a depth of about 5-7 μm after removing a surface layer of the as quenched samples by fine grounding and polishing. This guaranties the removal of both the oxide layer developed during water quenching and outer surface layer of high nitrogen concentration (~5 μm thick according to Figure 3). Analysis of the diffractograms revealed the presence of body-centered cubic (bcc) α for the unnitrided sample, while the face-centered cubic (fcc) γ is the only phase observed (within the information depth probed by XRD) for the SN-3H and SN-9H samples. The X-ray diffractogram of the SN-12H, SN-

13H, SN-18H samples shows predominantly austenite and weak additional peaks corresponding to the Cr_2N phase.

For the samples nitrided for 12h, 13h and 18h, the (111) and (220) austenite reflections have a small shoulder on the higher Bragg angle side. The main origins of this asymmetric broadening or side-bands occurrence for the diffraction peaks of SN-12H, SN-13H and SN-18H samples can be attributed to i) the presence of nano-sized and coherent precipitates [34, 35] and ii) development of local stress gradients due to the to the differences in grain to grain nitrogen depth profile originating from the anisotropy of nitrogen diffusion coefficient as well as from the nitrogen gradient inside the grains [36]. As, the present authors in their previous research article [37], via microstructure and microchemistry analysis near the austenite grain boundaries of full austenitic Fe-23Cr-2.4Mo-1.2N stainless steel by transmission electron microscopy (TEM-EDS) could not detect nitride precipitates around the austenite grain boundaries; asymmetric broadening of peaks in SN-12H, SN-13H and SN-18H samples most probably resulted from non-uniform volumetric expansion of the austenite lattice due to the nitrogen uptake. This result indicates the presence of regions with lower and higher nitrogen content in the SN-12H, SN-13H and SN-18H samples.

The lattice constants of the phases presented in the un-nitrided, partial nitrided (SN-3H), full austenitic (SN-9H), SN-12H, SN-13 and SN-18H samples were determined by using the WINPOW program [38]. The XRD results showed that chromium nitride precipitates in SN-12H, SN-13 and SN-18H samples has a hexagonal crystal lattice with lattice parameters of a=2.8048 Å and c=4.5074 Å. On the other hand, ferrite phase in the un-nitrided sample and austenite phase in the SN-3H sample have a cubic crystal structure

with lattice parameters of a=2.8831 Å and 3.6360 Å, respectively. Moreover, the lattice parameters of 3.6415 Å, 3.6426 Å, 3.6432 Å and 3.6434 Å were obtained for austenite phase in the SN-9H, SN-12H, SN-13H and SN-18 samples, respectively. The lattice parameter calculation results indicate that there is little change in the lattice parameter of austenite phase with solution nitriding time (about 0.15-0.20 %).

The obtained lattice parameter for nitride precipitates in this study is somewhat higher than that of experimentally measured for stoichiometric and pure hexagonal Cr_2N phase which is reported to be a=2.747 Å, c=4.439 Å and a=2.770 Å, c= 4.474 Å for nitrogen poor and nitrogen rich phases, respectively [39]. On the other hand, the obtained values are very close to the lattice parameters of a=2.84 Å and c=4.57 Å reported [39] for formation of mixed $CrMoN_X$ nitride in high temperature alloys. Therefore, the higher lattice parameter values in the present work could be related to incorporation of Mo atoms with greater atomic radius (145 pm) than Cr (140 pm) in formation of $(Cr, Mo)_2N$ nitride. The Mo concentration profile across the matrix/precipitate interface (see section 3.5) also confirms formation of $(Cr, Mo)_2N$ precipitates as nearly the same Mo content for matrix and precipitates was obtained by line scan EDS analysis.

3.3. Reflected light microscopy

A cross-sectional reflected light micrograph of the steel in the un-nitrided condition is shown in Figure 5. The base material exhibits one phase region (which has ferritic structure according to the XRD data in Figure 4) with an average grain size of about 130µm. Cross-sectional reflected light micrographs of the steel samples after solution nitriding for 3, 9, 12, 13 and 18 h are presented in Figure 6. After solution nitriding treatment for 3 hour, a new phase appears in the near surface region (Figure 6a), where nitrogen enters the sample

and its concentration is the highest (the ferrite-to-austenite transition, according to the XRD data presented in Figure 4). As a consequence of nitrogen uptake, austenite nucleated and grew from the specimen surface in an early stage of nitriding. Austenite (γ) and ferrite (α) phases are appeared as white and dark areas in Figure 6 (a), respectively. Also, it can be seen that the austenite layer is remained un-corroded but the ferrite layer is exhibited some degrees of corrosion during etching. This indicates high corrosion resistance of the austenite phase in the etchant reagent. Clearly, a relatively thick zone of approximately 450μm of austenite phase can be produced by solution nitriding for 3 h (Figure 6a). Increasing the nitriding time to 9 h (Figure 6b) resulted in a complete conversion of the ferrite core into austenite. Prolonging the solution nitriding time to 12, 13 and 18 h (Figure 6c,d ande) chromium-rich nitrides formed, firstly close to the surface (Figure 6c) and later throughout the sample (Figure 6d and e).

An overview of colonies of two-phase regions with a more or less lamellar morphology is shown for sample SN-13H in Figure 7. It appears that the colonies grow from austenite grain boundaries into the austenite grains (see arrows in Figure 7).

3.4. Scanning electron microscopy

SEM micrographs of the morphology of $(Cr,Mo)_2N$ precipitates are shown in Figure 8. For revealing the precipitate morphology the polished surface was deep-etched with 50% HCl+25% HNO_3+25% H_2O (vol. %). From the micrographs it appears that $(Cr,Mo)_2N$ has grown from the austenite grain boundaries (Figure 8a) with a rod or strip-like morphology (Figure 8b) most probably with a discontinuous precipitation mechanism, see section 4.

3.5. Transmission electron microscopy

A bright field TEM image and selected area diffraction pattern (SADP) of a rod or strip-like chromium-rich nitride precipitate at the centre of the SN-13H sample are shown in Figure 9a and 9b, respectively. The selected area diffraction pattern recorded from the nitride allowed identification as $(Cr,Mo)_2N$. The SADP corresponding to an area within the austenite phase shows γ-Fe reflections compatible with an $\left[1\bar{1}0\right]_{\gamma}$ electron beam zone axis and $(Cr,Mo)_2N$ reflections compatible with $\left[1\bar{1}0\right]_{(Cr,Mo)_2N}$ electron beam zone axis. The $(Cr,Mo)_2N$ precipitates obey the following orientation relation with the austenite matrix (see Figure 9c):

$$(002)_{(Cr,Mo)_2N} // (111)_{\gamma}, \left[1\bar{1}0\right]_{(Cr,Mo)_2N} // \left[1\bar{1}0\right]_{\gamma} \quad (1)$$

The above orientation relationship is close to the relationship reported in the literature between the $(Cr,Mo)_2N$ and austenite phases [15, 40]. For a more detailed analysis, the microchemistry across the austenite/nitride precipitate interface was investigated with energy-dispersive X-ray spectroscopy (EDS) line scans in scanning TEM (STEM) mode. Figures 10 (a) and 10 (b) show the STEM image and the chemical composition profiles for iron, chromium and molybdenum across the austenite/nitride precipitate interface at the centre of the SN-13H sample. The STEM-EDS chemical composition profile in Figure 10b shows a chromium content of about 80 wt. % (of the metallic composition) in $(Cr,Mo)_2N$, which confirms partitioning of iron and chromium during $(Cr,Mo)_2N$ precipitation. Within experimental accuracy no change in molybdenum content was observed between the adjoining phases. This is consistent with an anticipated

slower diffusivity of Mo as compared to Fe and Cr. Based on the STEM-EDS analysis, the chemical composition of the $(Cr,Mo)_2N$ strips is $(Cr_{0.83}Fe_{0.14}Mo_{0.03})_2N$. It is expected that Fe and Mo can be dissolved into Cr_2N, as both Fe and Mo form nitrides isomorphous with Cr_2N. Thermodynamically, both Fe and Mo are weaker nitride formers than Cr, which explains their relatively low contents as compared to Cr.

3.6. Electron Back Scatter Diffraction

Since the $(Cr,Mo)_2N$ precipitates are several hundred nanometers in size, it was difficult to determine and analyze the growth mechanism of precipitates using TEM. Therefore, for more detailed studies EBSD analysis was performed instead. SEM micrograph obtained on a region containing $(Cr,Mo)_2N$ precipitates (discontinuous precipitation) in the sample SN-13H and the corresponding EBSD map is presented in Figure 11. The grains having the different crystallographic orientation exhibit the different colour in Figure 11 (b) and (c). Clearly, the orientation of austenite in the regions containing $(Cr,Mo)_2N$ deviates from the neighbouring austenite grains (Figure 11 (b)), indicating coupled growth of $(Cr,Mo)_2N$ and austenite. However, this should be studied in more details.

Within a transformed region small variations in austenite orientation occur (Figure 11 (c)). These small variations could not be shown to be related to small angle grain boundaries. Rather a change of the morphology of $(Cr,Mo)_2N$ is suggested by Figure 11 (c). This change of morphology is likely to be related to the growth mode of the transforming region. As can be seen from Figure 11 (c), the as-measured orientation distribution of $(Cr,Mo)_2N$ precipitates appears to change between two orientation, colour coded as yellow (marked by 1) and pink (marked by 2). This result could be related to different variants of same crystallographic orientation relationship between austenite and $(Cr,Mo)_2N$ nitride.

4. Discussion

Evaluation of cross-sectional microstructures according to Figure 6 (c)-(e), revealed that the $(Cr,Mo)_2N$ phase with discontinuous precipitation mechanism formed in supersaturated austenite with a high chromium equivalent (about 25%) at a high nitriding temperature of 1473K (1200°C). The chromium equivalent (Cr_{eq}) was calculated using the following equation which is used to construct the Schaeffler diagram [41]:

$$Cr_{\text{equivalent}}\,(\text{in wt. \%}) = \%Cr + \%Mo + 1.5\%Si + 0.5\%Nb + 2\%\,Ti \qquad (2)$$

Classical discontinuous (or cellular) precipitation is usually described as the nucleation of a second phase from supersaturated solution on a grain boundary and breakthrough of one grain into the other so that the discontinuous precipitation colony grows into one grain with the matrix phase having the same orientation as the grain that "breaks through the grain boundary" [42]. The main feature of discontinuous precipitation is that the grain boundary shifts with the growing tips of the precipitates and that partitioning of the species is generally occurred by diffusion through the moving boundary. As compared to the classical discontinuous precipitation, in the present case discontinuous precipitation is not only a decomposition of a supersaturated solution, but simultaneously the nitrogen content in the alloy increases during the transformation (see Figure 2). Also, in the studied Fe-Cr-N alloy unlike the classical discontinuous precipitation, the austenite phase has no preferred orientation relation to the austenite grains in the transformed regions wherein the discontinuously transformed region grows (Figure 11).

The mechanism for discontinuous precipitation in Fe-Cr-N does not only involve the partitioning of substitution dissolved elements through the moving boundary, but bulk

diffusion of the interstitially dissolved nitrogen is likely to proceed through the bulk. Consequently, nitrogen can be exchanged with the environment, either as an additional uptake (as for the present case) or by nitrogen release (see for example [43]), depending on whether binding all chromium to chromium-rich nitride leads to a higher or lower nitrogen content than in the precursor supersaturated solid solution. Discontinuous precipitation has repeatedly been reported for the ferritic Fe-Cr-N system [19-21, 23, 26] as well as for the austenitic Fe-Cr-N system [15-18], including stainless steels with a colossal nitrogen content. Here, a distinction is made between discontinuous precipitation in ferritic and austenitic alloys. The overall reaction describing discontinuous precipitation in *ferritic* alloys is given by:

$$\alpha_{ss}\text{+CrN (coherent)} \rightarrow \alpha_{s}\text{ +CrN (lamella)} \quad (3)$$

Where α_{ss} and α_{s} denote super-saturated ferrite and saturated ferrite with nitrogen, respectively. The reaction describes the replacement of initially fine coherent CrN precipitates by a lamellae-like CrN under continued nitriding and simultaneous elimination of the super-saturation of excess nitrogen from ferrite. This type of reaction was observed during gas or plasma nitriding of Fe-Cr alloys [19-24]. Mortimer et al. [19] studied the effects of Cr content and nitriding potential between 773K (500°C) and 1273K (1000°C) on the stability of CrN and Cr_2N in gaseous nitriding of Fe-Cr binary alloys. They reported that CrN is the stable nitride for alloys with less than 20 wt % Cr. For alloys containing more than 20 wt. % Cr, Cr_2N is formed at high temperatures and CrN develops at lower temperatures. The overall reaction describing discontinuous precipitation in *austenitic* alloys is given by:

$$\gamma_{ss} \rightarrow \gamma_s + Cr_2N \quad (4)$$

Where γ_{ss} and γ_s denote super-saturated austenite and saturated austenite with nitrogen, respectively. The reaction involves decomposition of supersaturated austenite into nitrogen-depleted austenite and lamellae-like Cr_2N phase. This type of reaction has been observed during aging of HNASSs at 973-1223K (700-950°C) [15-18]. The morphology of Cr_2N precipitates via a discontinuous precipitation mechanism depends on the aging time and temperature. For example, Feng et al. [18] reported that the morphology of cellular Cr_2N precipitates in Fe-18Cr-12Mn-0.48N austenitic steel changed from initially granular to lamellar with increasing aging time in the temperature range 973-1223K (700-950°C).

In order to check that the discontinuous precipitation colonies growth occurs under uptake of more nitrogen or by just decomposition, the fully solution nitrided sample (SN-9H) was subjected to annealing heat treatment at 1200°C under argon gas atmosphere for 9 hours. Figure 12 shows the optical micrograph and X-ray diffraction pattern of cross-section of fully nitride sample (SN-9H) after annealing at 1200°C for 9 hours under argon gas atmosphere. According to Figure 12 (a), it can be seen that annealing resulted in the evolution of equiaxed grains. The XRD pattern (Figure 12 (b)) revealed the disappearing of the austenite phase and formation of the ferrite phase in the microstructure of annealed SN-12H sample. Thus, it can be concluded that the growth of the colonies in the present study is not only driven by the precipitation from supersaturated solution but occurs through the continued nitrogen uptake. Therefore, in the present study, unlike discontinuous precipitation in ferritic Fe-Cr-N alloys; the discontinuous precipitation transformation is not preceded by a stage where homogeneous precipitation of Cr-nitride occurs. Thus, the following mechanism suggests itself. Discontinuous precipitation in the present alloy is

most likely initiated by the nucleation of $(Cr,Mo)_2N$ at grain boundaries; where after new austenite nucleates onto $(Cr,Mo)_2N$. This would be consistent with the images in Figures 7 and 11, which show that growth of the discontinuous precipitation colonies starts from grain boundaries and proceeds into the neighbouring grains, rather than by the "breakthrough" of one austenite grain into another. Moreover, this mechanism can explain that the crystallographic orientation of austenite in the transformed colony has no orientation relation to the austenite in the neighbouring grains. The partitioning of Fe and Cr that is necessary for growth of the transformed colony is proceeding through the moving boundary between the discontinuous colony and the untransformed austenite grains. Nitrogen is likely to be supplied to the advancing transformation front through the bulk of the (un)transformed austenite grains and along the $(Cr,Mo)_2N$/austenite interfaces. Moreover, it should be noted that the growth mechanism of $(Cr,Mo)_2N$ precipitates at 1473K (1200°C) in this study is more complex than the mechanism at lower temperatures, because austenite grains grow concurrently with the progress of the discontinuous precipitation.

5. Conclusion

In this study the precipitation of chromium nitride after austenite super-saturation was investigated during high temperature solution nitriding (1200 °C) in pressurized gas (2.5 bars) for prolonged time (18 h). Microstructural features of precipitates were investigated by means of TEM and EBSD to determine the chemical composition, morphology and crystallography of the precipitates and also the matrix/precipitate orientation relationship. The results obtained are summarized as follows:

(1) Chromium-rich nitride ($(Cr,Mo)_2N$ type) precipitates develop on prolonged solution nitriding by a discontinuous precipitation mechanism as rod or strip-like morphology; the transformation commences from austenite grain boundaries, where Cr_2N is expected to nucleate first.

(2) $(Cr,Mo)_2N$ rods/strips have an ordered structure and exhibit a $(002)_{(Cr,Mo)_2N} // (111)_\gamma$, $\left[1\bar{1}0\right]_{(Cr,Mo)_2N} // \left[1\bar{1}0\right]_\gamma$ orientation relationship with austenite.

(3) EBSD studies on the discontinuously precipitated colonies revealed that, austenite in the transformed regions has no crystallographic orientation relation to the adjacent untransformed austenite.

(4) The growth of discontinuous precipitation colonies occurs under the uptake of nitrogen from the nitriding gas and not by a mere decomposition of supersaturated austenite.

Acknowledgements

The authors would like to thank Thomas L. Christiansen, H. Alimedadi and Steffen S. Munch, Department of Mechanical Engineering and Center for Electron Nanoscopy of Denmark Technical University, for access to the laboratories and simulating discussion and their fruitful comments.

References

[1] M. Sumita, T. Hanawa, and S.H. Teoh, *Development of nitrogen-containing nickel-free austenitic stainless steels for metallic biomaterials—review*, Mater. Sci. Eng. C 24 (2004), pp. 753–760.

[2] L. Montanaro, M. Cervellati, and D. Campoccia, *Promising in vitro performances of a new nickel-free stainless steel*, J. Mater. Sci. Mater. Med. 17 (2006), pp. 267–275.

[3] J.A. Disegil and L. Eschbachz, *Stainless steel in bone surgery*, Injury. 31 (2000), pp. D2–D6.

[4] Y.N. Turan and A. Koursarist, *Nitrogen-alloyed austenitic stainless steels and their properties*, J. South. Afr. Inst. Min. Metall. 93 (1993), pp. 97–104.

[5] L. Reclaru, R. Ziegenhagen, P.Y. Eschler, A. Blatter, and J. Lemaître, *Comparative corrosion study of "Ni-free" austenitic stainless steels in view of medical applications*, Acta Biomater. 2 (2006), pp. 433–444.

[6] K. Yang and Y. Ren, *Nickel-free austenitic stainless steels for medical applications*, Sci. Technol. Adv. Mater. 11 (2010), pp. 1–13.

[7] A.P. Tschiptschin, C.H. Aidar, F.B. Neto, and N. Alonso-Fallerios, *Nitrogen bearing austenitic stainless steels for surgical implants*, Mater. Sci. Forum 318-320 (1999), pp. 569–578.

[8] H. Berns and S. Siebert, *High nitrogen austenitic cases in stainless steels*, ISIJ Int. 36 (1996), pp. 927–931

[9] H. Berns, J.W. Bouwman, U. Eul, J. Izagirre, R.L. Juse, H.J. Niederau, G. Tavernier, and R. Zieschang, *Solution nitriding of stainless steels for process engineering*, Mat.-wiss. u. Werkstofftech 31 (2000), pp. 152–161.

[10] H. Berns, B. Edenhofer, and R. Zaugg, *Industrial experience with case hardening of stainless steels by solution nitriding*, Trans. Mater. Heat. Treat. 25 (2004), pp. 354–359.

[11] H. Berns and A. Kühl, *Reduction in wear of sewage pump through solution nitriding*, Wear 256 (2004), pp. 16–20.

[12] J.W. Simmons, *Overview: high-nitrogen alloying of stainless steels*, Mater. Sci. Eng. A 207 (1996), pp. 159–169.

[13] J.C. Rawers, J.S. Dunning, G. Asai, and R.P.Reed, *Characterization of stainless steels melted under high nitrogen pressure*, Metall. Trans. A 23 (1992), pp. 2061–2068.

[14] G. Balachandran, M.L. Bhatia, N.B. Ballal, and P. Krishna, *Some theoretical aspects on designing nickel free high nitrogen austenitic stainless steels*, ISIJ Int. 41 (2001), pp. 1018–1027.

[15] P.A. Carvalho, I.F. Machado, G. Solórzano, and A.F. Padilha, *On Cr_2N precipitation mechanisms in high-nitrogen austenite*, Philos. Mag. 88 (2008), pp. 229–242.

[16] R.D. Knutsen, C. I. Lang, and J. A. Basson, *Discontinuous cellular precipitation in a Cr–Mn–N steel with niobium and vanadium additions*, Acta Mater. 52 (2004), pp. 2407–2417.

[17] L. Rovatti, R. Montanari, N. Ucciardello, A. Mezzi, S. Kaciulis, and A. Carosi, *Discontinuous precipitation in a high-nitrogen austenitic steel*, Mater. Sci. Forum 638-642 (2010), pp. 3597–3602.

[18] S. Feng, W. Li-jun, C. Wen-fang, and L. Chun-ming, *Precipitation kinetics of Cr_2N in high nitrogen austenitic stainless steel*, J. Iron Steel Res. Int. 15 (2008), pp. 72–77.

[19] B. Mortimer, P. Grieveson, and K. H. Jack, *Precipitation of Nitrides in Ferritic Fe Alloys Containing Cr*, Scand. J. Metall. 1 (1972), pp. 203–209.

[20] P.M. Hekker, H.C.F. Rozendaal, and E.J. Mittemeijer, *Excess nitrogen and discontinuous precipitation in nitrided iron-chromium alloys*, J. Mater. Sci. 20 (1985), pp. 718–729.

[21] R.E. Schacherl, P.C.J. Graat, and E.J. Mittemeijer, *Gaseous nitriding of iron-chromium alloys*, Z. Metallkd. 93 (2002), pp. 468–477.

[22] M. Sennour, P.H. Jouneau, and C. Esnouf, *TEM and EBSD investigation of continuous and discontinuous precipitation of CrN in nitrided pure Fe-Cr alloys*, J. Mater. Sci. 39 (2004), pp. 4521–4531.

[23] G. Miyamoto, A. Yonemoto, Y. Tanaka, T. Furuhara, and T. Maki, *Microstructure in a plasma-nitrided Fe–18 mass% Cr alloy*, Acta Mater. 54 (2006), pp. 4771–4779.

[24] G. Miyamoto, Y. Tomio, H. Aota, K. Oh-ishi, K. Hono, and T. Furuhara, *Precipitation of nanosized nitrides in plasma nitrided Fe–M (M= Al, Cr, Ti, V) alloy*s, Mater. Sci. Technol. 27 (2011), pp. 742–746.

[25] R.G. Baker and J. Nutting, *Precipitation processes in steels*, Iron Steel Inst. Spec. Rep. 64 (1959), pp. 1–22.

[26] E.J. Mittemeijer, A.B.P Vogels, and P.J. Van Der Schaaf, *Morphology and lattice distortions of nitrided iron and iron-chromium alloys and steels*, J. Mater. Sci. 15 (1980), pp. 3129–3140.

[27] P.C. van Wiggen, H.C.F. Rozendaal, and E.J. Mittemeijer, *The nitriding behavior of iron-chromium-carbon alloys*, J. Mater. Sci. 20 (1985), pp. 4561–4182.

[28] T. Tsuchiyama, H. Ito, K. Kataoka, and S. Takaki, *Fabrication of ultrahigh nitrogen austenitic steels by nitrogen gas absorption into solid solution*, Metall. Mater. Trans. A 34 (2003), pp. 2591–2599.

[29] D. Kuroda, T. Hanawa, T. Hibaru, S. Kuroda, M. Kobayashi, and T. Kobayashi, *New manufacturing process of nickel-free austenitic stainless steel with nitrogen absorption treatment*, Mater. Trans. 44 (2003), pp. 414–420.

[30] T. Tscuchiyama, H. Uchida, K. Katako, and S. Takaki, *Fabrication of fine-grained high nitrogen austenitic steels through mechanical alloying treatment*, ISIJ Int. 42 (2002), pp. 1438–1443.

[31] H. Mitsui and S. Kurihana, *Solution nitriding treatment of Fe–Cr alloys under pressurized nitrogen gas*, ISIJ Int. 47 (2007), pp. 479–485.

[32] R. Mohammadzadeh and A. Akbari, *Effect of pressurized solution nitriding on phase changes and mechanical properties of ferritic Fe–22.7 Cr–2.4 Mo stainless steel*, Mater. Sci. Eng. A 592 (2014), pp. 153–163.

[33] *Thermo-Calc software AB*, Stockholm, Sweden, 2000; software available at http://www.thermocalc.com

[34] H. Selg, E. Bischoff, I. Bernstein, T. Woehrle, S. R. Meka, R. E. Schacherl, T. Waldenmaier, and E.J. Mittemeijer, *Defect-dependent nitride surface layer development upon nitriding of Fe–1 at. % Mo alloy*, Philos. Mag. 93 (2013), pp. 2133–2160.

[35] T. Steiner, M. Akhlaghi, S.R. Meka, and E.J. Mittemeijer, *Diffraction-line shifts and broadenings in continuously and discontinuously coarsening precipitate-matrix systems: coarsening of initially coherent nitride precipitates in a ferrite matrix*, J. Mater. Sci. 50 (2015), pp. 7075–7086.

[36] A. Martinavičius, G. Abrasonis, W. Möller, C. Templier, J. P. Rivière, A. Declémy, and Y. Chumlyakov, *Anisotropic ion-enhanced diffusion during ion nitriding of single crystalline austenitic stainless steel*, J. Appl. Phys. 105 (2009), pp. 1–7.

[37] R. Mohammadzadeh, A. Akbari, and M. Mohammadzadeh, *Impact Toughness Properties of Nickel-and Manganese-Free High Nitrogen Austenitic Stainless Steels*, Metall. Mater. Trans. A 47 (2016), pp. 6032–6041.

[38] D.B. Wiles and R.A. Young, *A new computer program for Rietveld analysis of X-ray powder diffraction patterns*, J. Appl. Crystallogr. 14 (1981), pp. 149–151.

[39] W.B. Pearson, *A Handbook of Lattice Spacings and Structures of Metals and Alloys*. Volume 4: International Series of Monographs on Metal Physics and Physical metallurgy, Elsevier, 2013.

[40] A.J. Ramirez, J.C. Lippold, and S.D. Brandi, *The relationship between chromium nitride and secondary austenite precipitation in duplex stainless steels*, Metall. Mater. Trans. A 34 (2003), pp. 1575–1597.

[41] W.F. Smith, *Structure and Properties of Engineering Alloys*, 2nd ed., McGraw-Hill, Inc., New York, 1993.

[42] D.A. Porter and K.E. Easterling, *Phase Transformation in Metals and Alloys*, 2nd ed., Chapman & Hall, London, 1992.

[43] F. Vanderschaeve, R. Taillard, and J. Foct, *Discontinuous precipitation of Cr_2N in a high nitrogen, chromium-manganese austenitic stainless steel*, J. Mater. Sci. 30 (1995), pp. 6035–6046.

Table 1. Chemical composition of Fe-Cr-Mo steel prepared in this investigation (all contents in wt. %).The chemical composition was determined by optical emission spectroscopy analysis using a SpectroLab M5 analyzer.

C	Cr	Ni	Mn	Mo	Si
≤0.002	22.753	0.045	0.100	2.420	0.052
Cu	Al	N	P	S	Fe
≤0.50	0.05	0.030	0.010	0.007	balance

Figure captions:

Figure 1. Calculated vertical section phase diagram of Fe-22.7Cr-2.4Mo-N alloy system at nitrogen partial pressure of (a) 0.1MPa and (b) 0.25MPa using the Thermocalc software and TCFE6 database.

Figure 2. Nitrogen content average of the steel plate samples before and after pressurized solution nitriding at 1473K (1200°C) and P_{N2}=2.5 bar for different times of 9h, 13h, and 18h.

Figure 3. GDOES nitrogen depth profiles at different solution nitriding time of 3, 9 and 12 hours (SN-3H, SN-9H and SN-12H samples).

Figure 4. XRD patterns recorded from the surface of the (a) base material, (b) SN-3H, (c) SN-9H, (d) SN-12H, (e) SN-13Hand (f) SN-18H samples.

Figure 5. Optical micrograph of Fe-22.7Cr-2.4Mo alloy.

Figure 6. Cross-sectional optical microstructure of Fe-22.7Cr-2.4Mo ferritic stainless steel after solution nitriding at 1473K (1200°C) and P_{N2}=2.5 bar for different nitriding times of (a) 3, (b) 9, (c) 12, (d) 13, and (e) 18h.

Figure 7. Optical micrograph of chromium nitrides precipitates in SN-13H sample.

Figure 8. Scanning electron micrograph of polished cross section in back-scatter imaging mode (a) and of deep-etched cross section in secondary electron imaging mode (b) of chromium nitrides at the centre of the SN-13H sample.

Figure 9. TEM image of rod or strip-like $(Cr,Mo)_2N$ precipitate at the centre of the SN-13H sample: (a) bright-field image, (b) selected area diffraction pattern, and (c) the corresponding indexation.

Figure 10. STEM image of $(Cr,Mo)_2N$ precipitate (a), and chemical composition depth profiles across the $(Cr,Mo)_2N$/austenite interface region at the centre of the SN-13H sample (b).

Figure 11. (a) Cross-sectional SEM micrograph of SN-13H sample, showing $(Cr,Mo)_2N$ discontinuous precipitation, (b) EBSD map of the austenite phase in the same region as in (a) and (c) as measured orientation map of $(Cr,Mo)_2N$ and austenite in the red box shown in (a).

Figure 12. Optical micrograph (a) and X-ray diffractogram (b) from cross-section of SN-9H sample after annealing heat treatment at 1200°C under argon gas atmosphere for 9 hours.

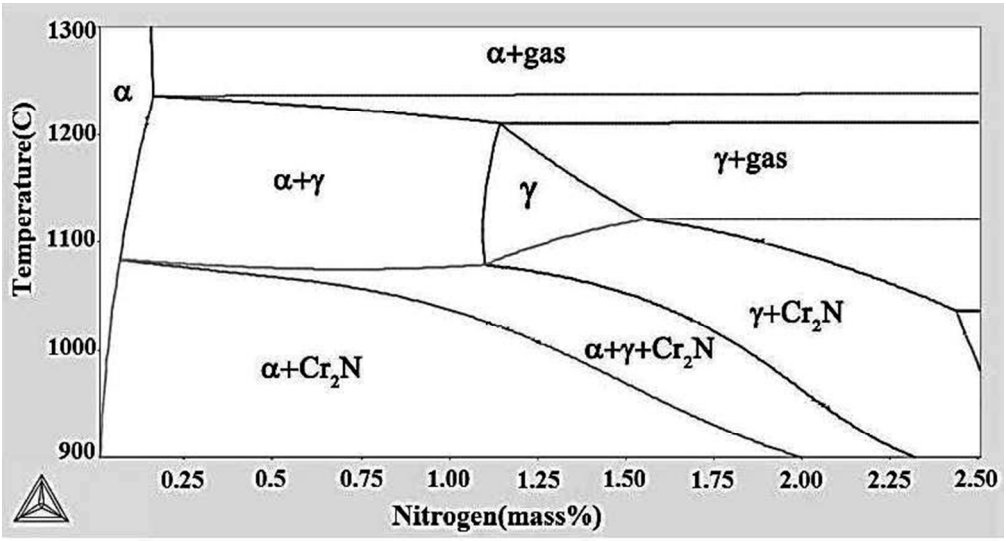

Fig. 1a

185x98mm (112 x 113 DPI)

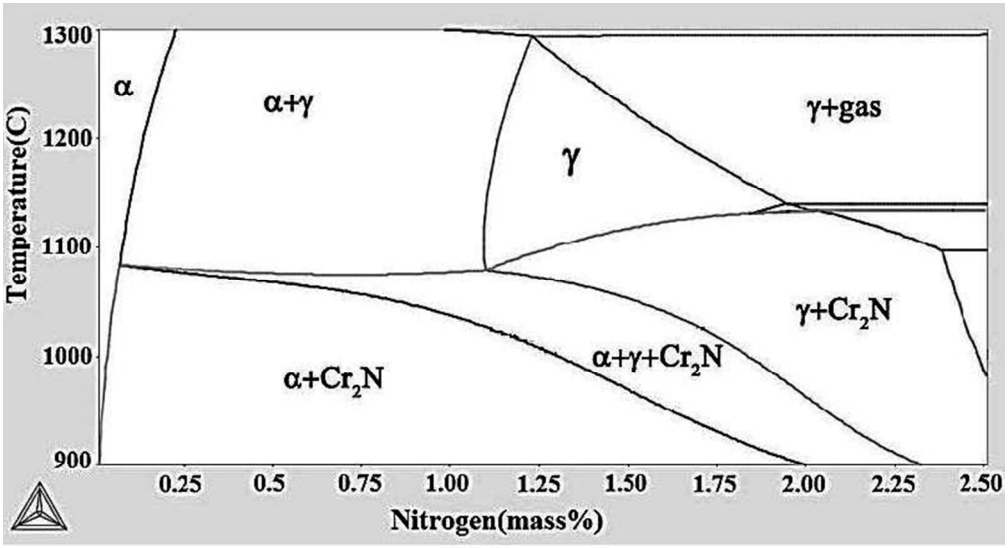

Fig. 1b

182x99mm (112 x 113 DPI)

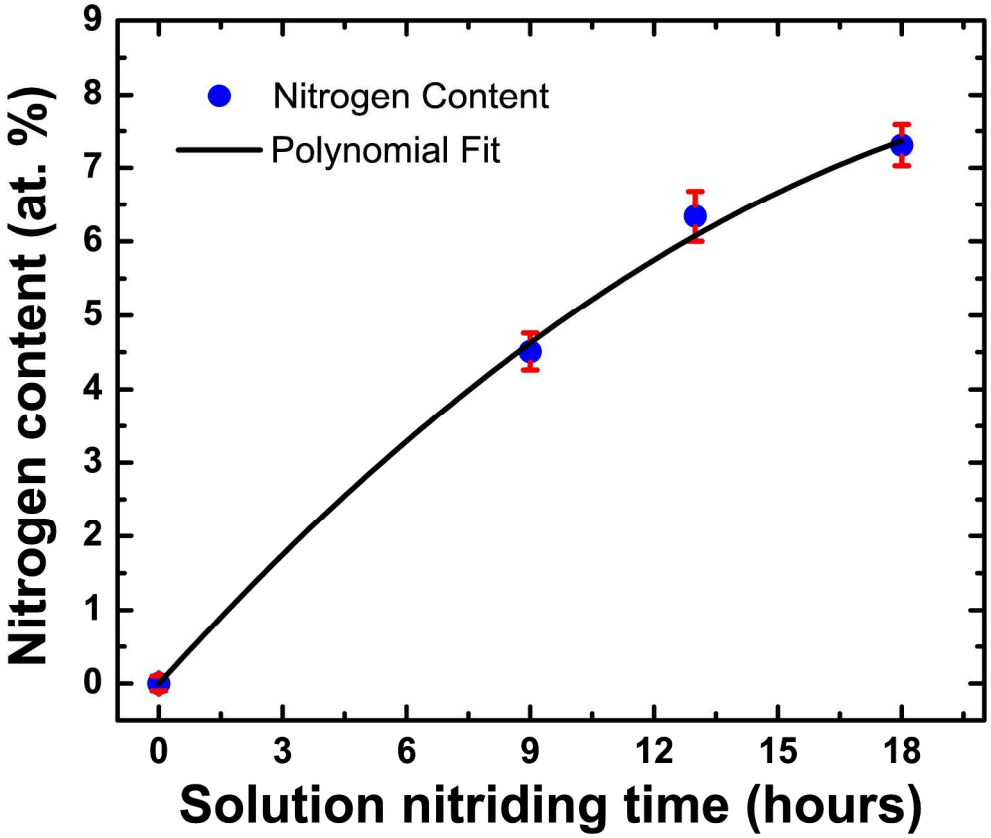

Fig. 2

228x192mm (300 x 300 DPI)

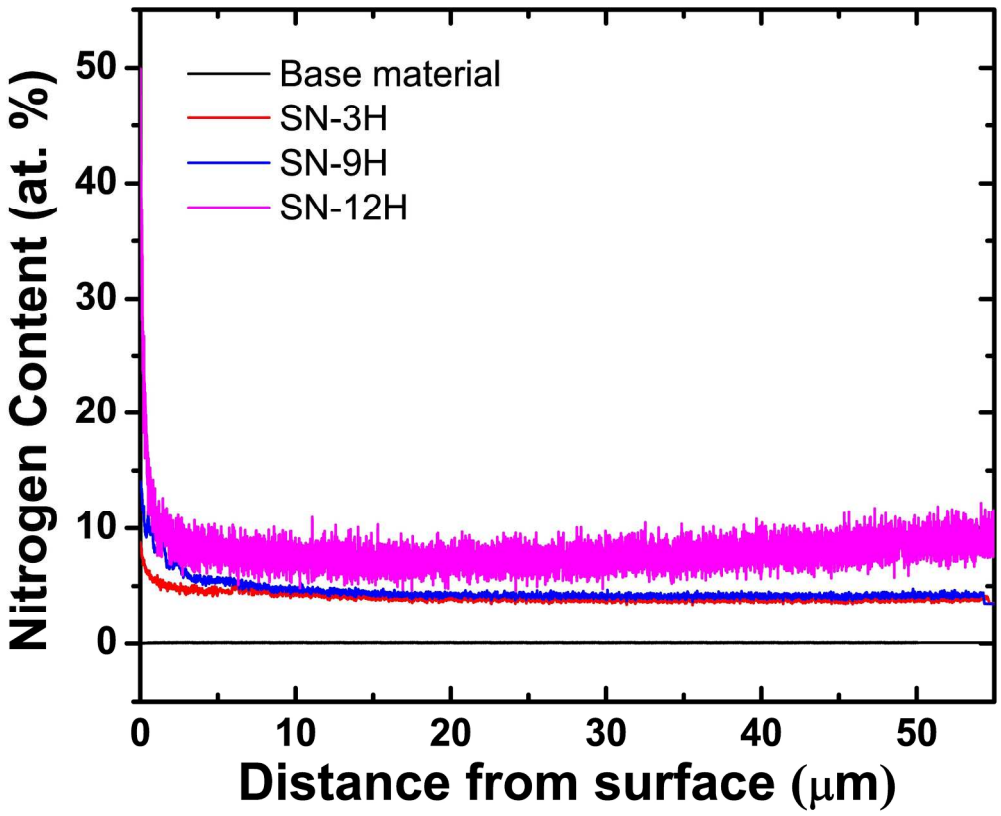

Fig. 3

217x175mm (300 x 300 DPI)

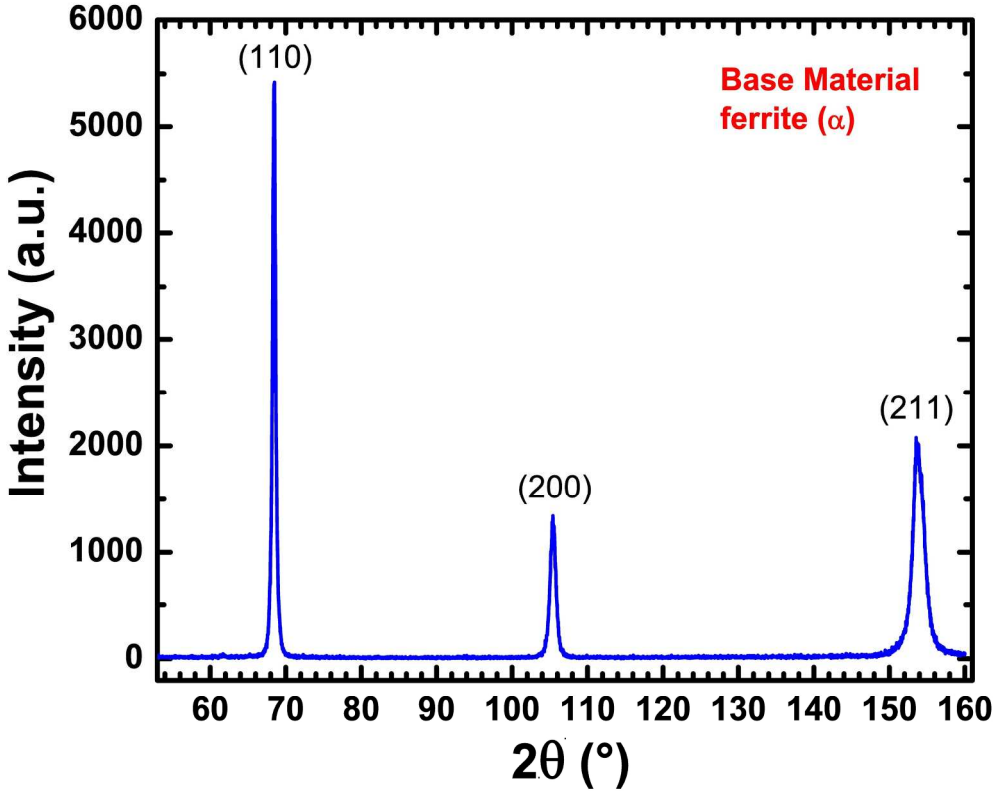

Fig. 4a

215x172mm (300 x 300 DPI)

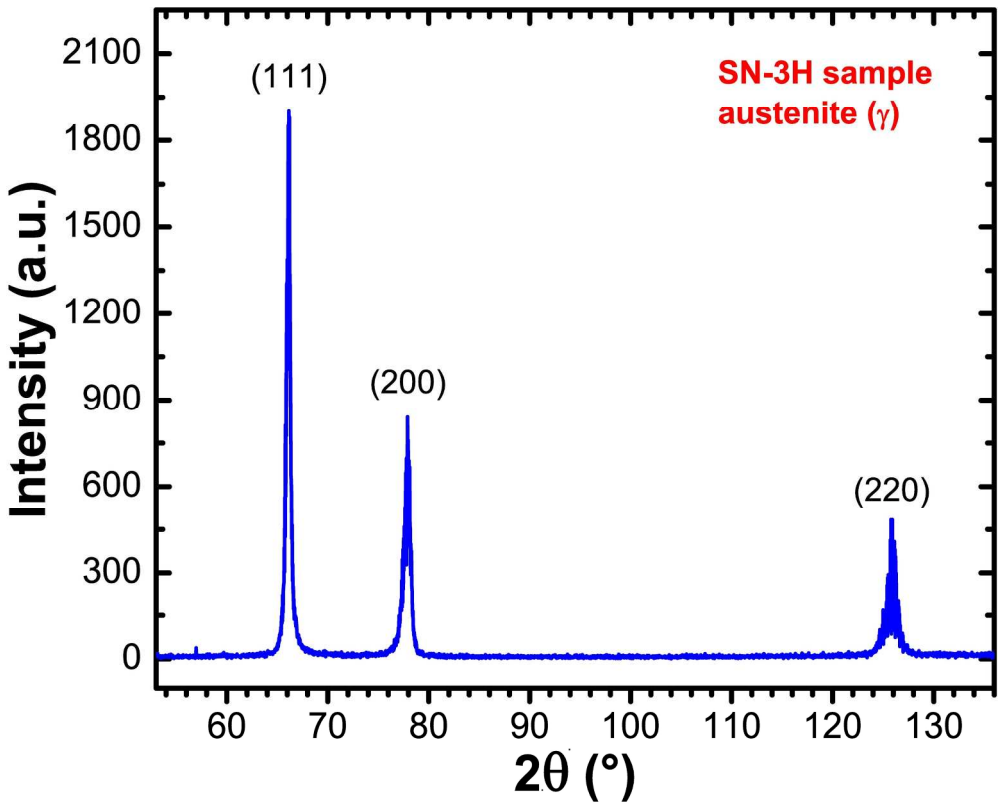

Fig. 4b

216x173mm (300 x 300 DPI)

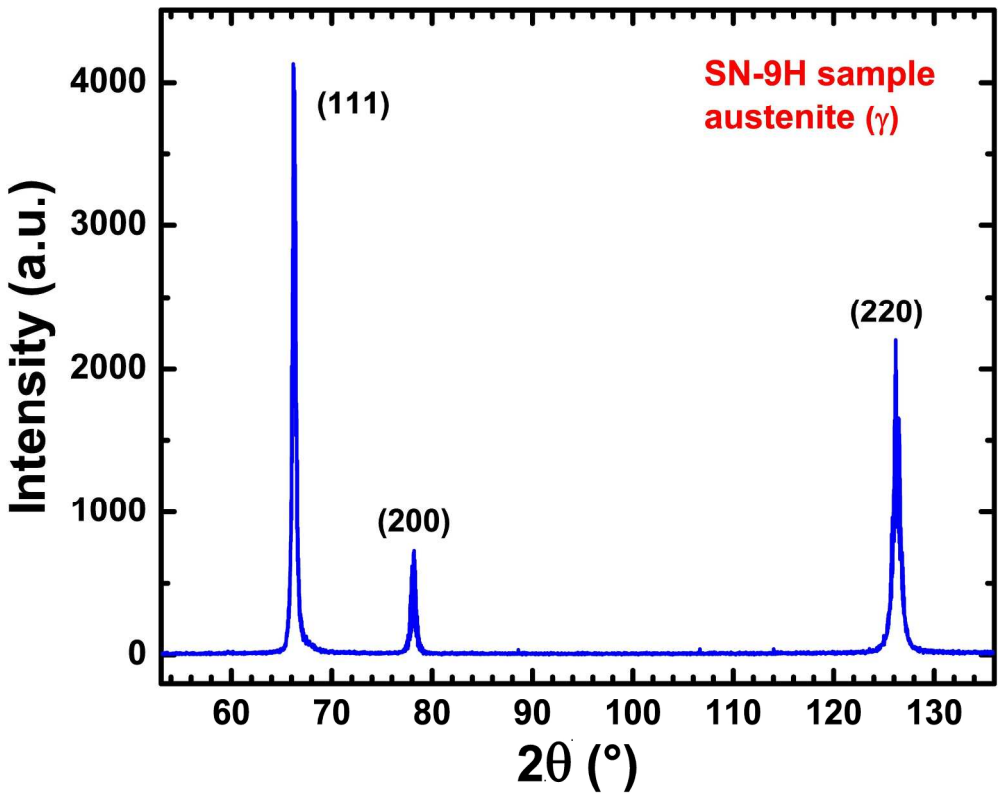

Fig. 4c

213x169mm (300 x 300 DPI)

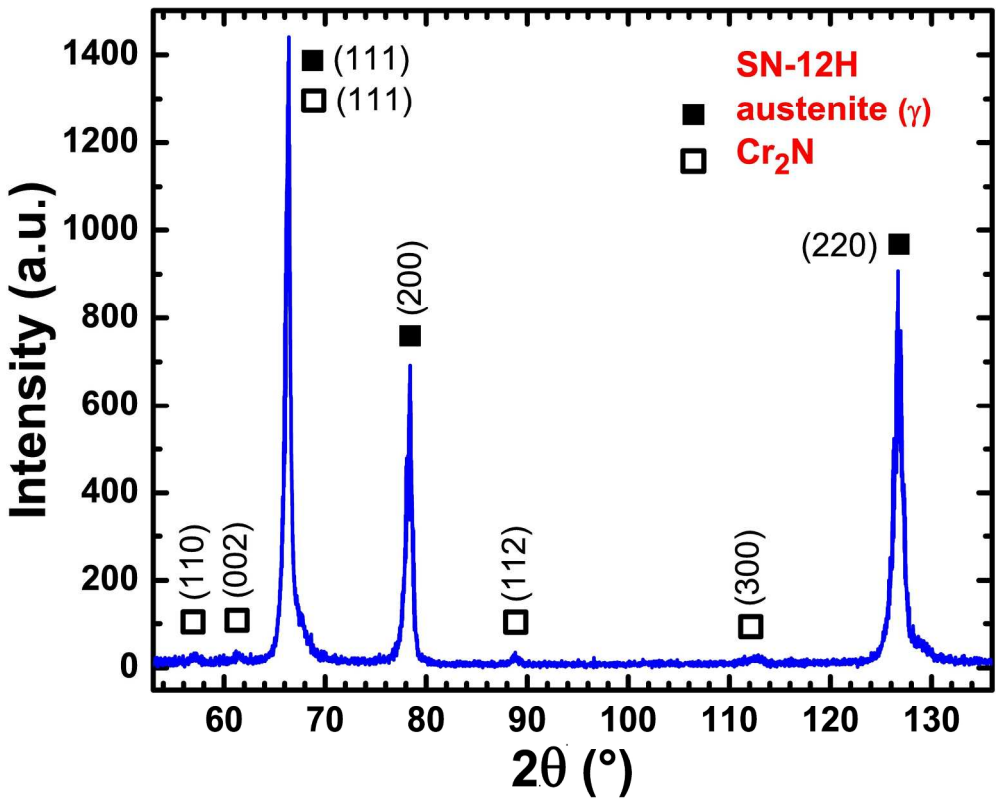

Fig. 4d

215x172mm (300 x 300 DPI)

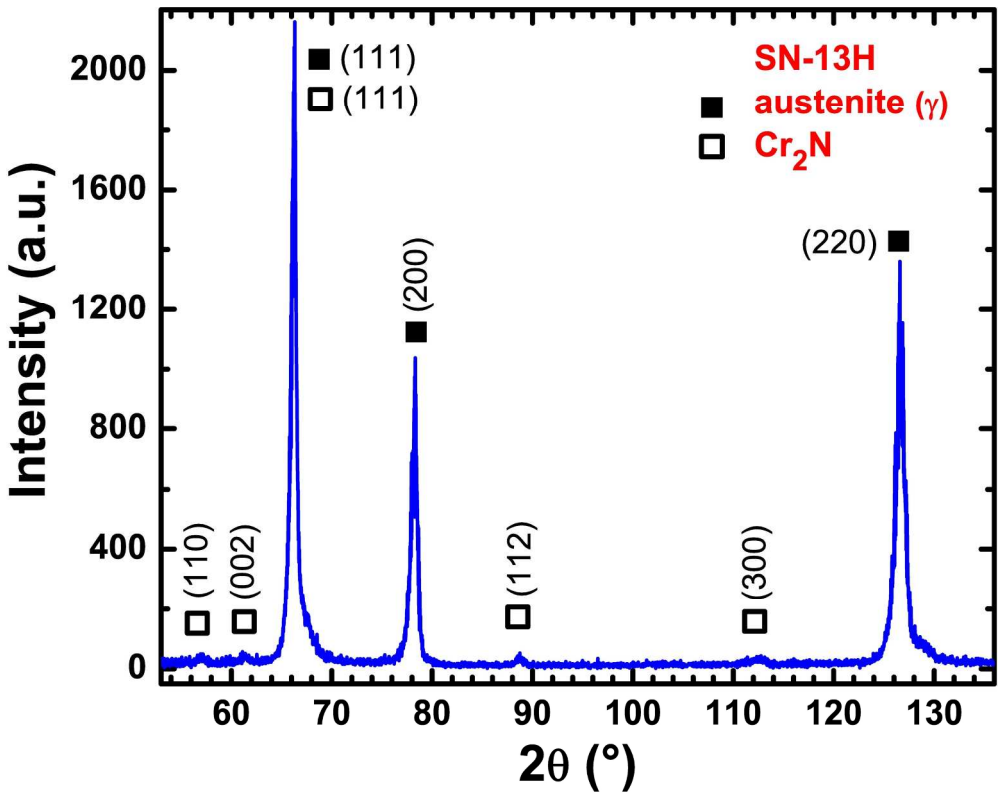

Fig. 4e

213x167mm (300 x 300 DPI)

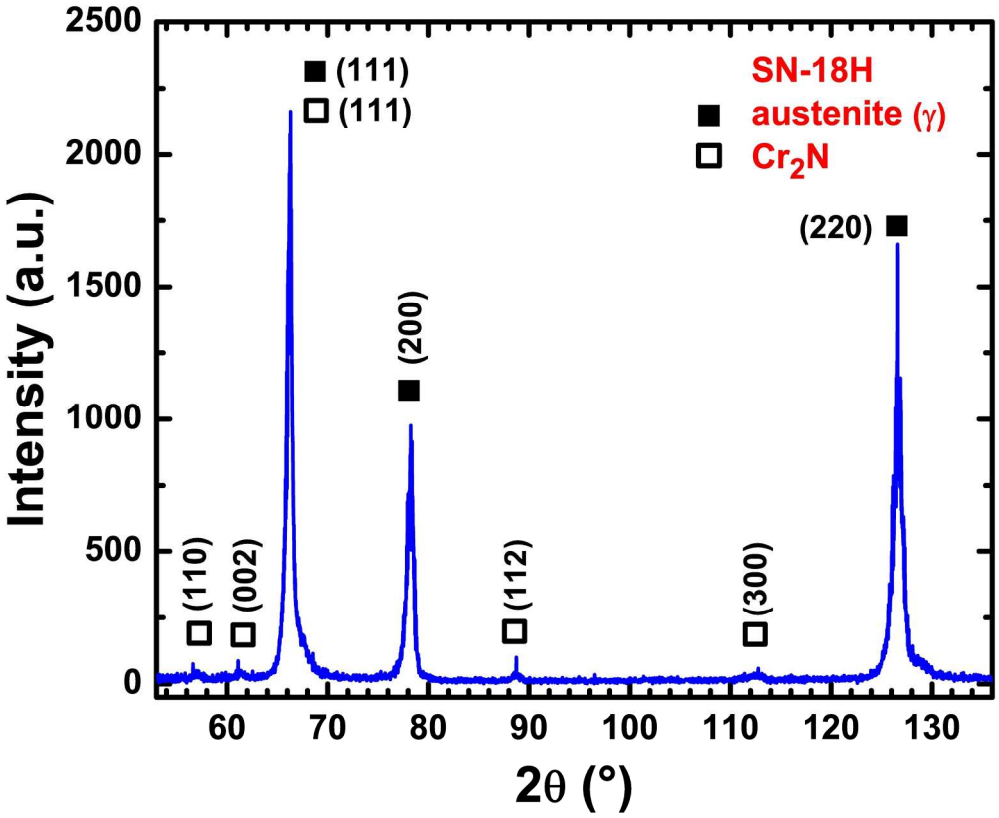

Fig. 4f

222x182mm (300 x 300 DPI)

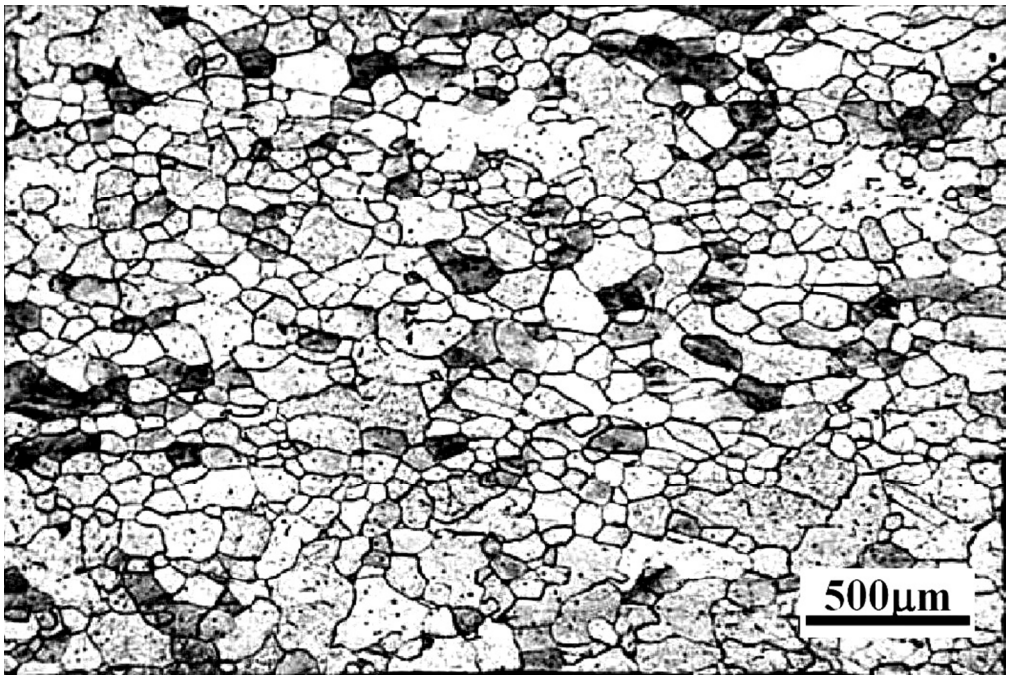

Fig. 5

277x185mm (96 x 96 DPI)

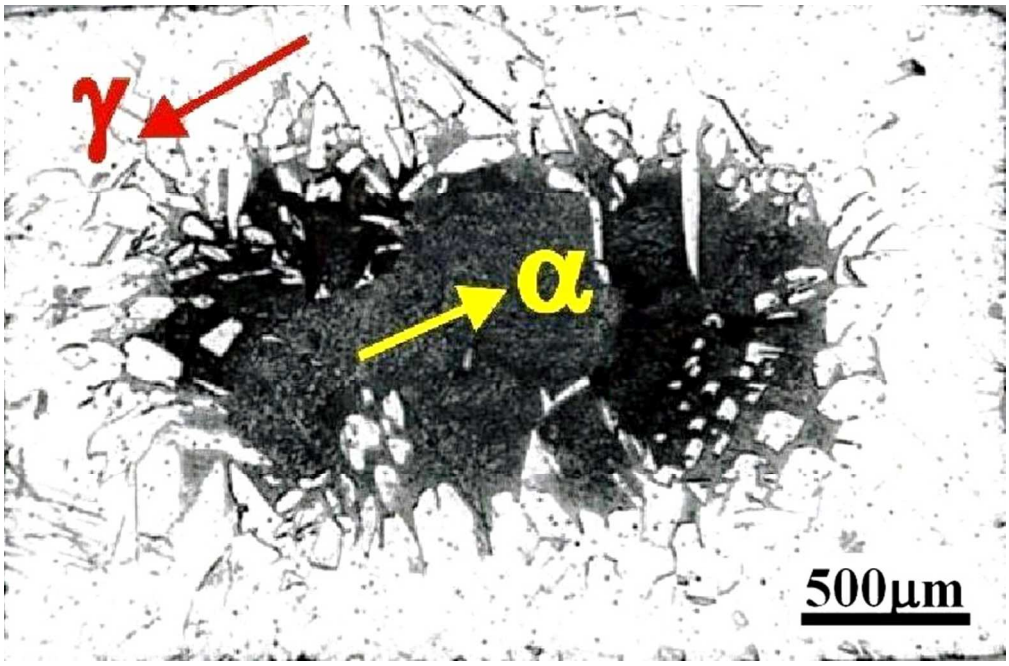

Fig. 6a

221x145mm (96 x 96 DPI)

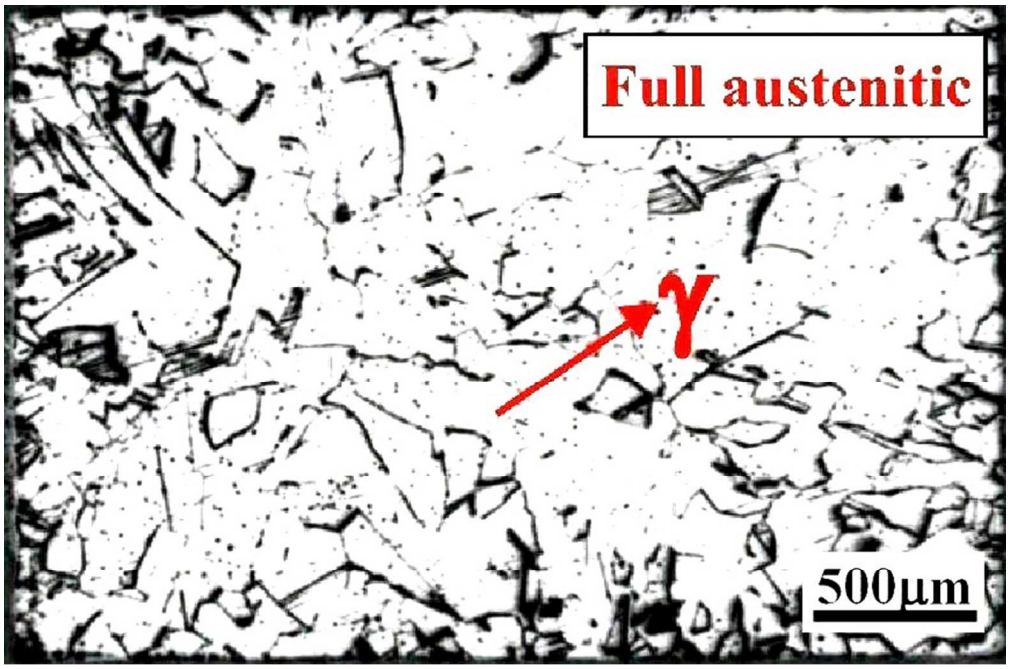

Fig. 6b

228x150mm (96 x 96 DPI)

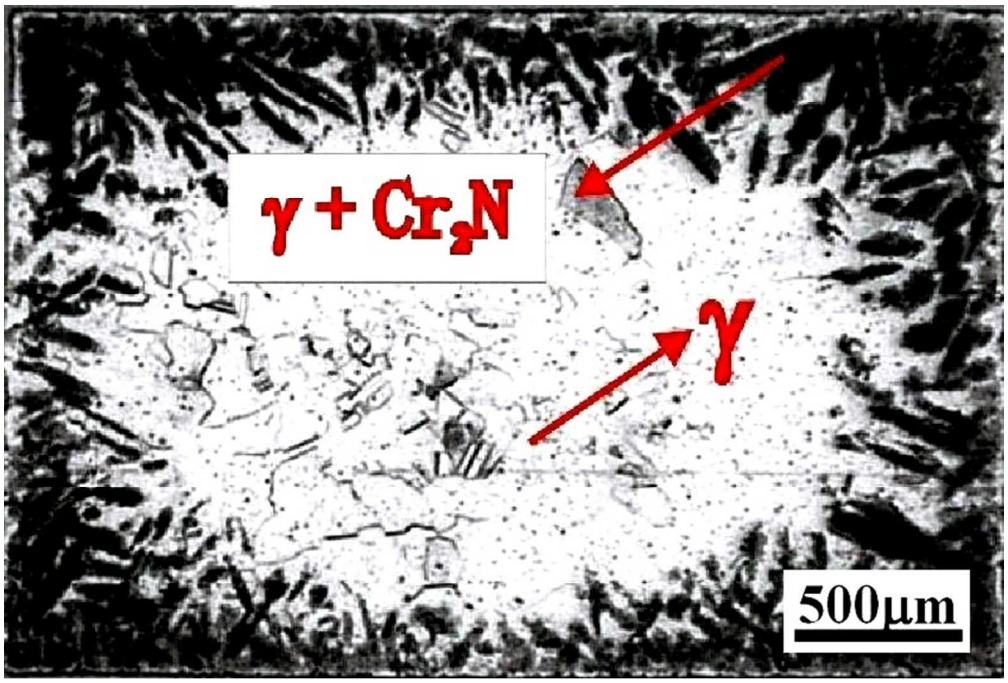

Fig. 6c

222x149mm (96 x 96 DPI)

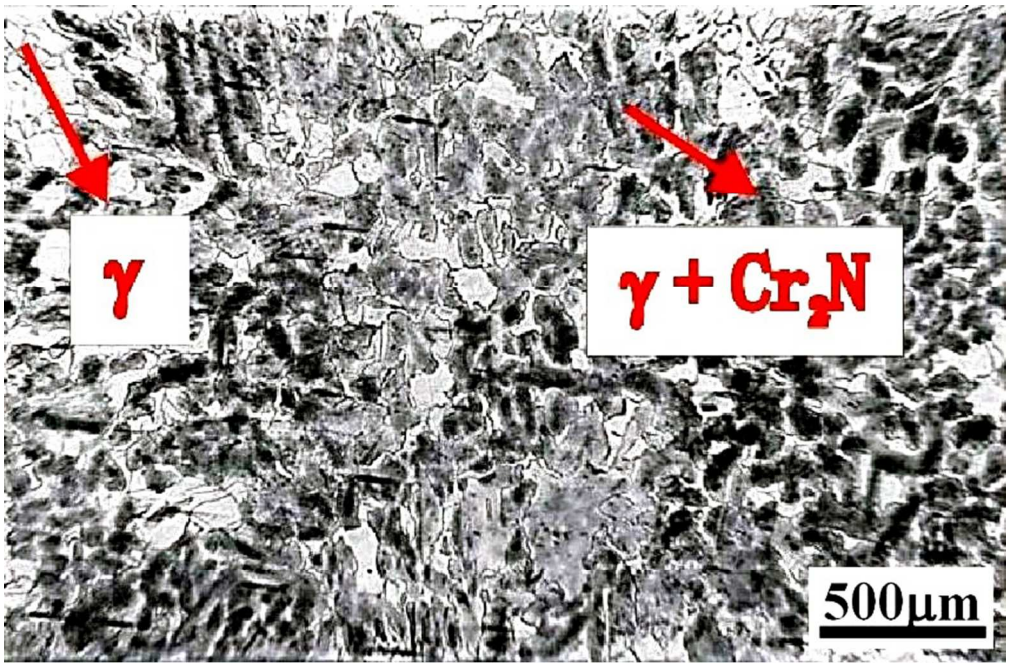

Fig. 6d

225x147mm (96 x 96 DPI)

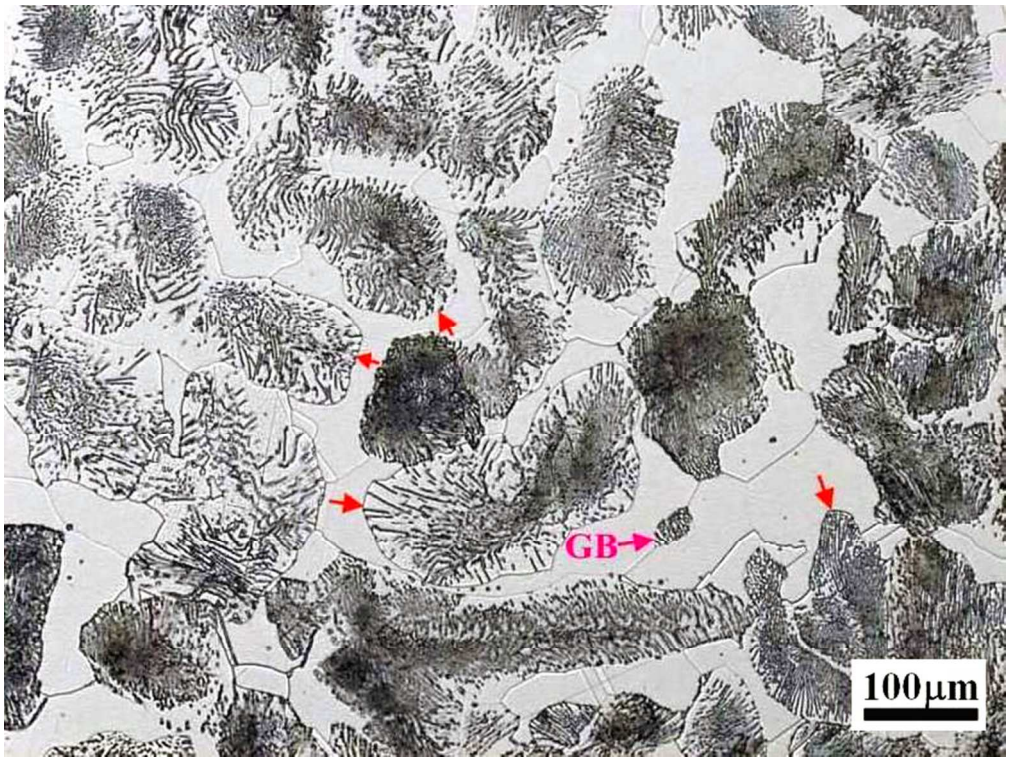

Fig. 7

219x164mm (96 x 96 DPI)

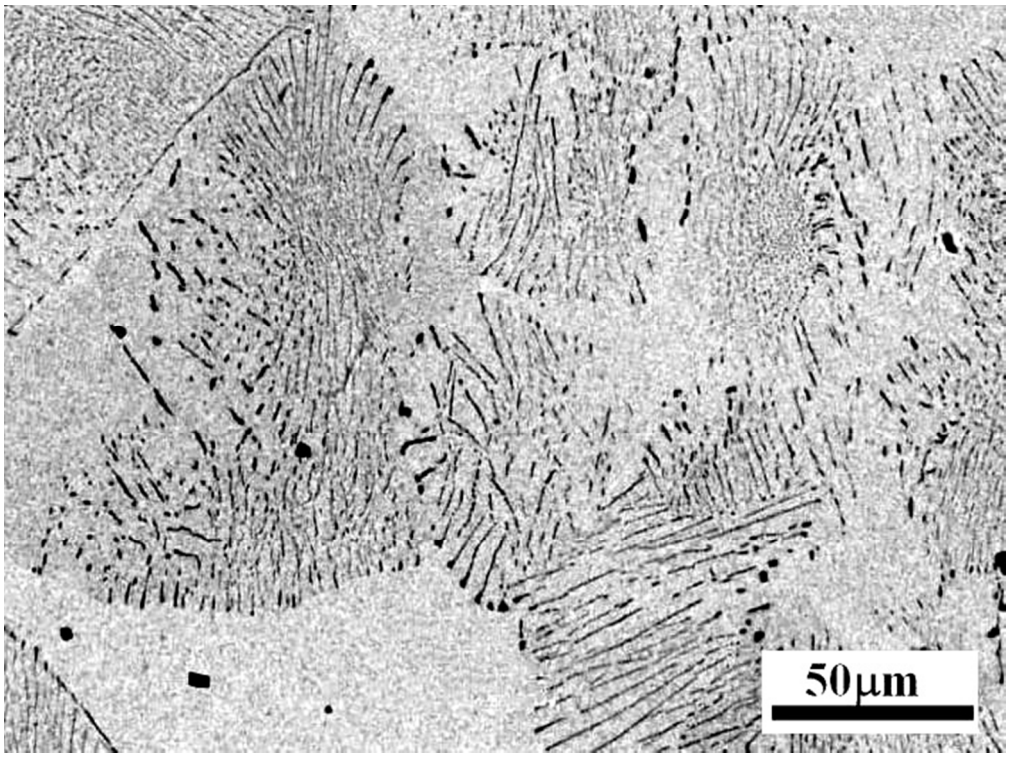

Fig. 8a

186x139mm (96 x 96 DPI)

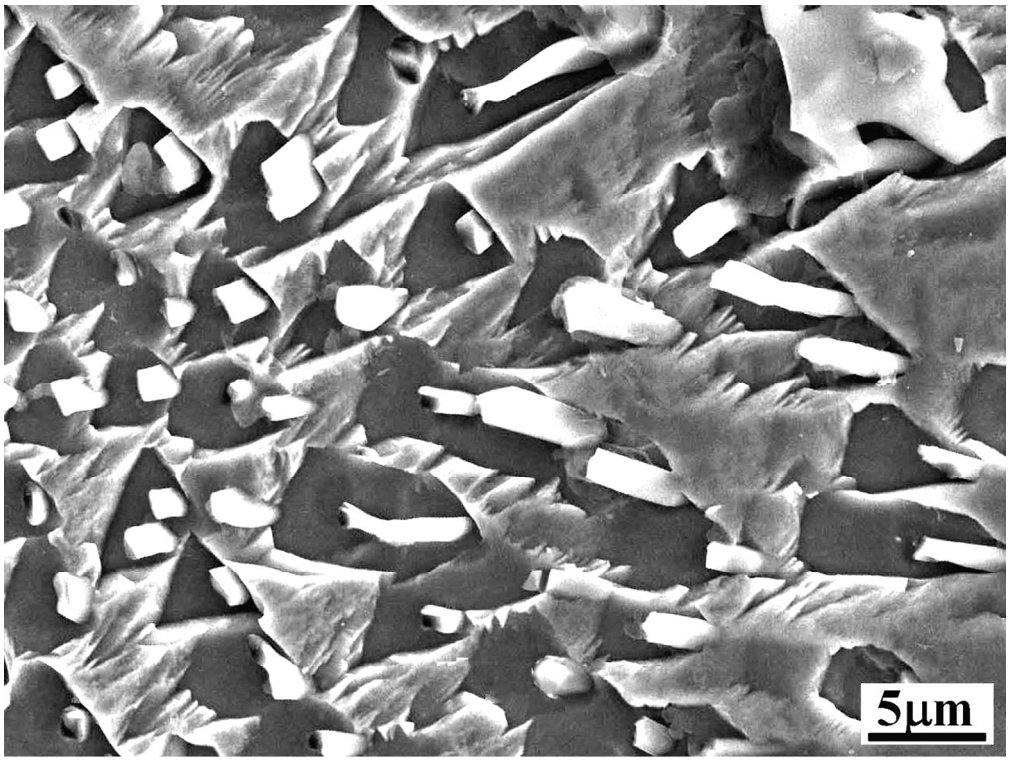

Fig. 8b

337x254mm (96 x 96 DPI)

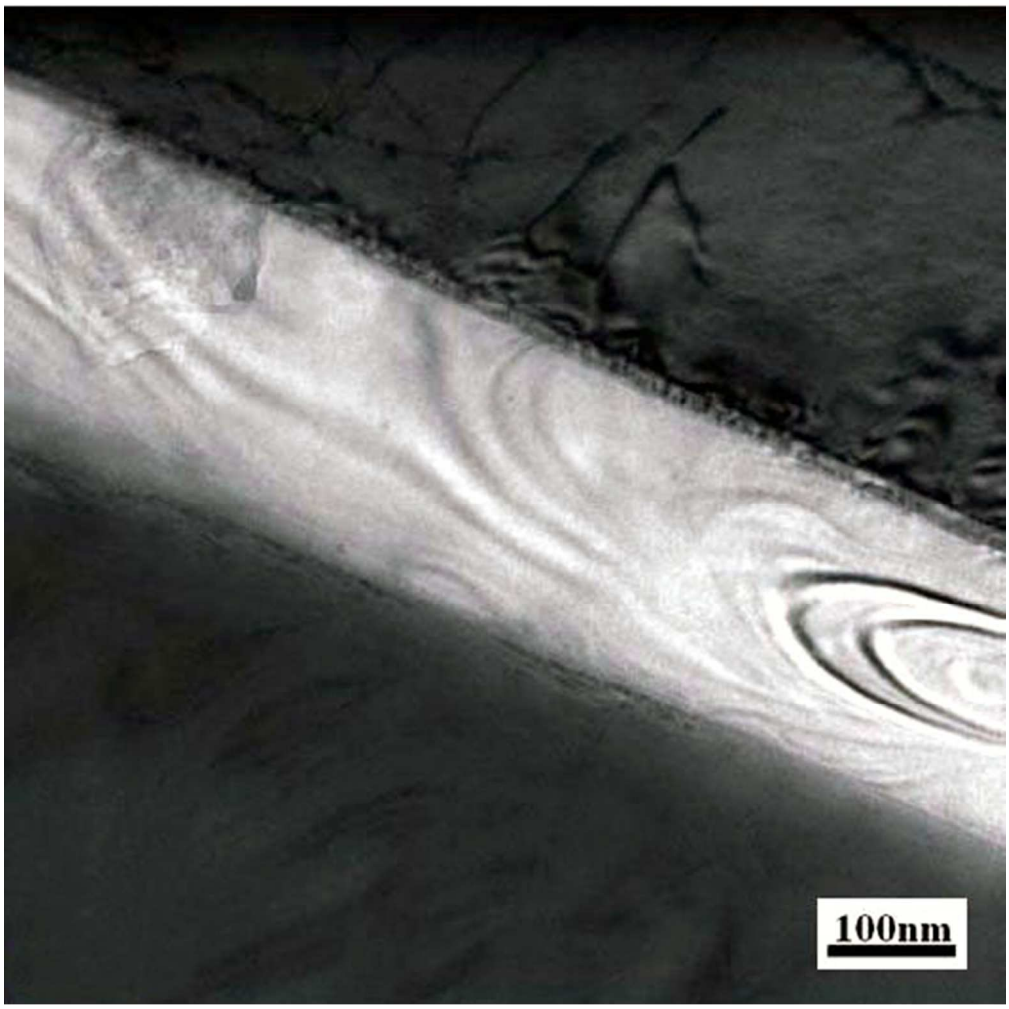

Fig. 9a

139x140mm (96 x 96 DPI)

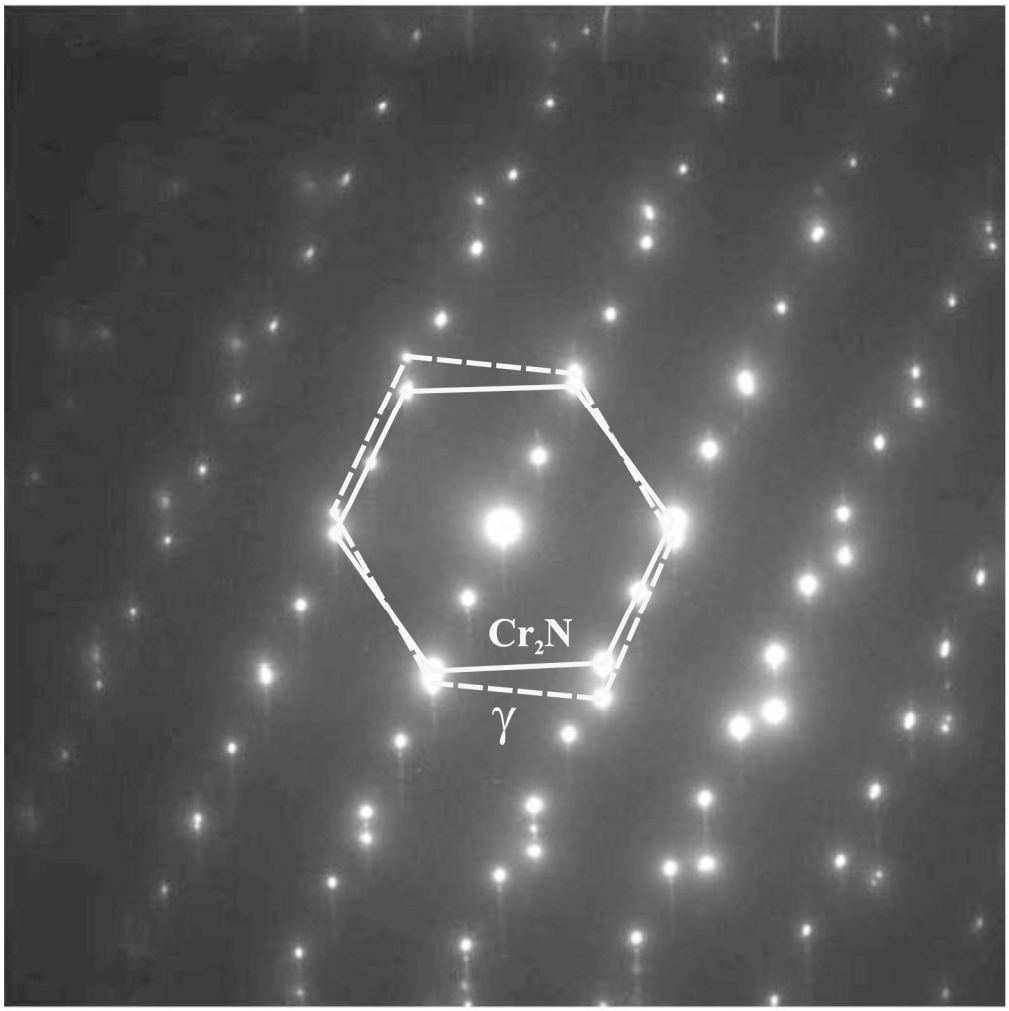

Fig. 9b

213x215mm (300 x 300 DPI)

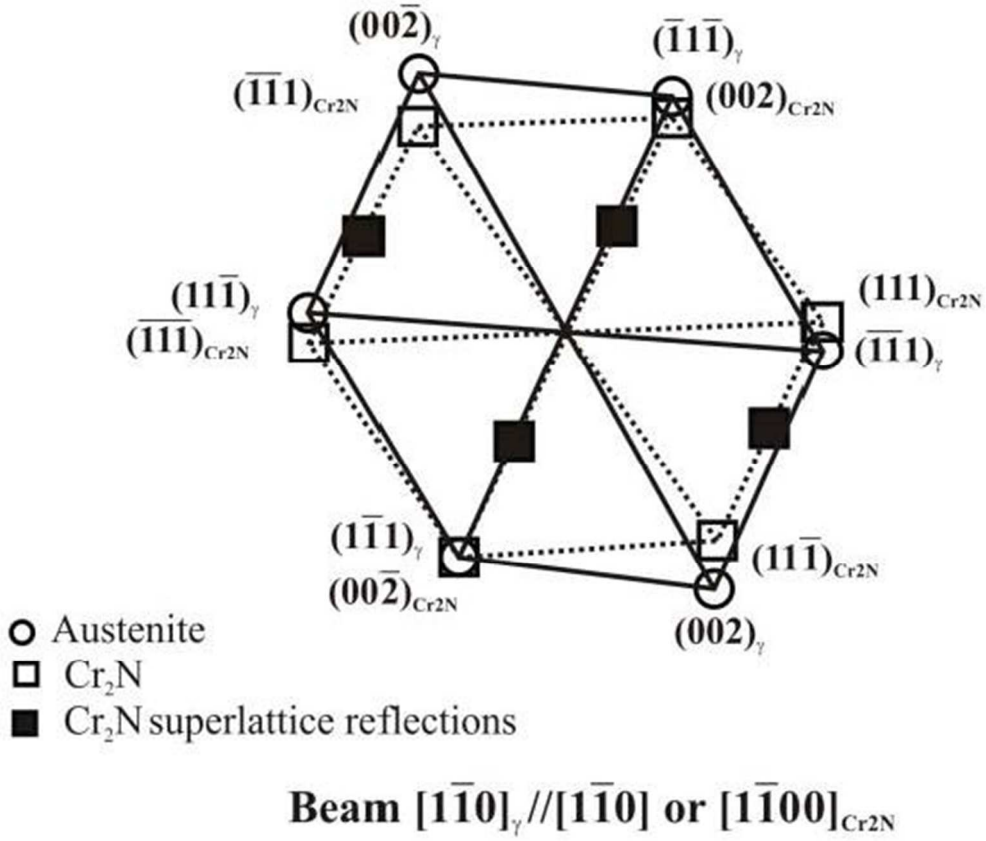

Fig. 9c

189x166mm (75 x 76 DPI)

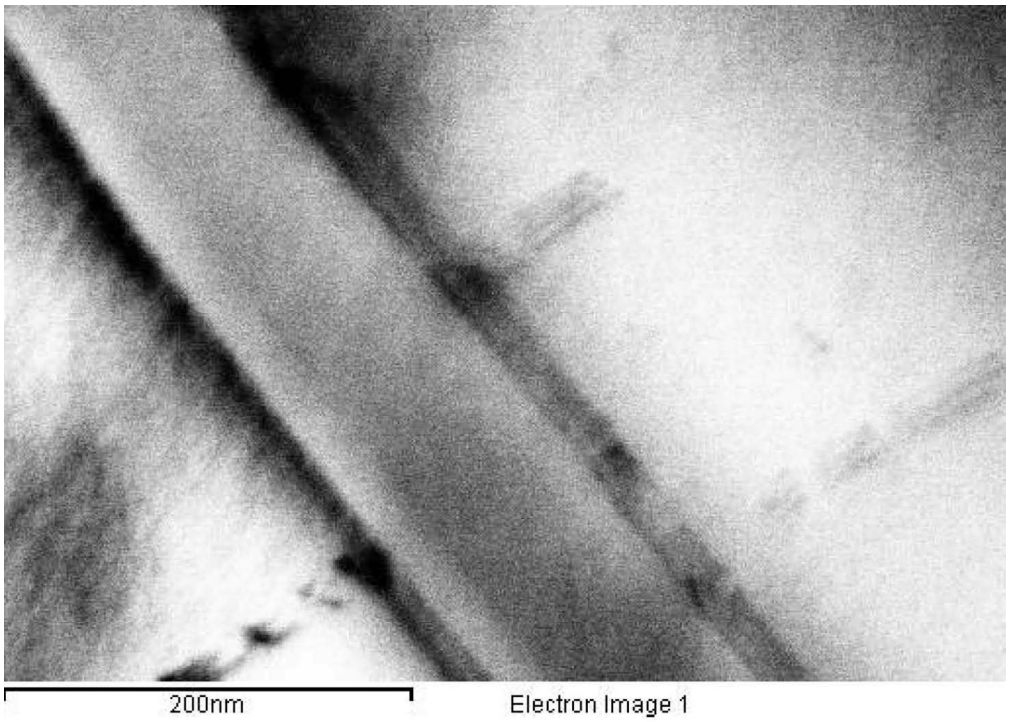

Fig. 10a

185x133mm (200 x 200 DPI)

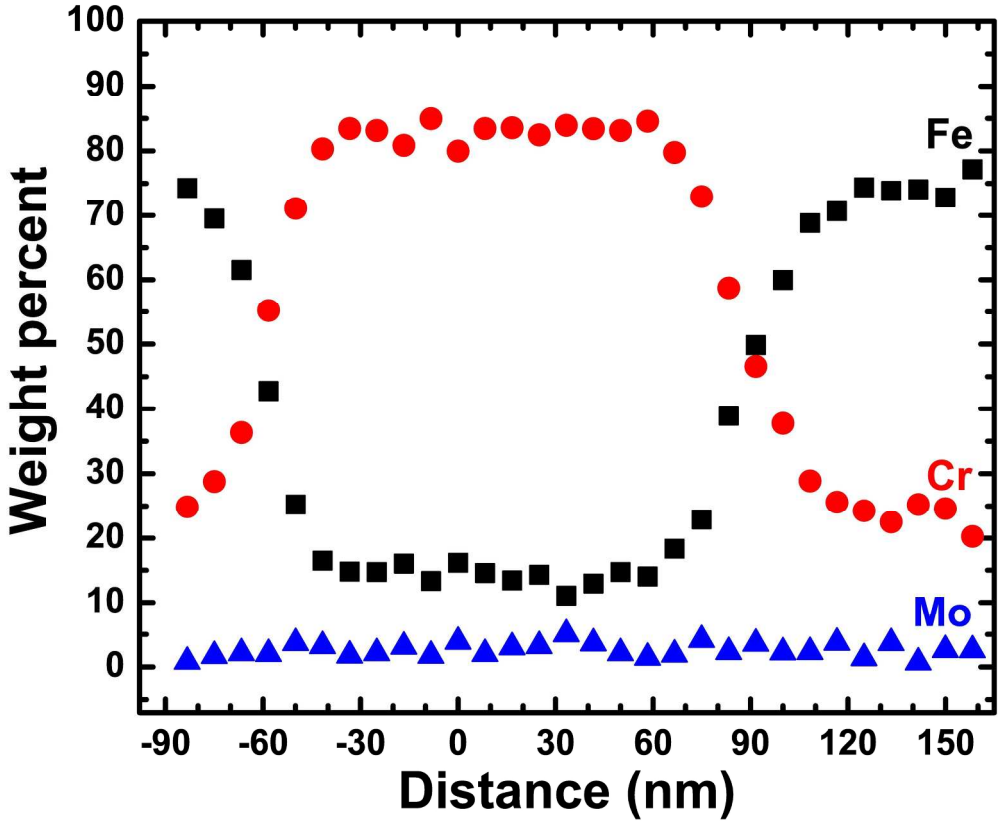

Fig. 10b

223x185mm (300 x 300 DPI)

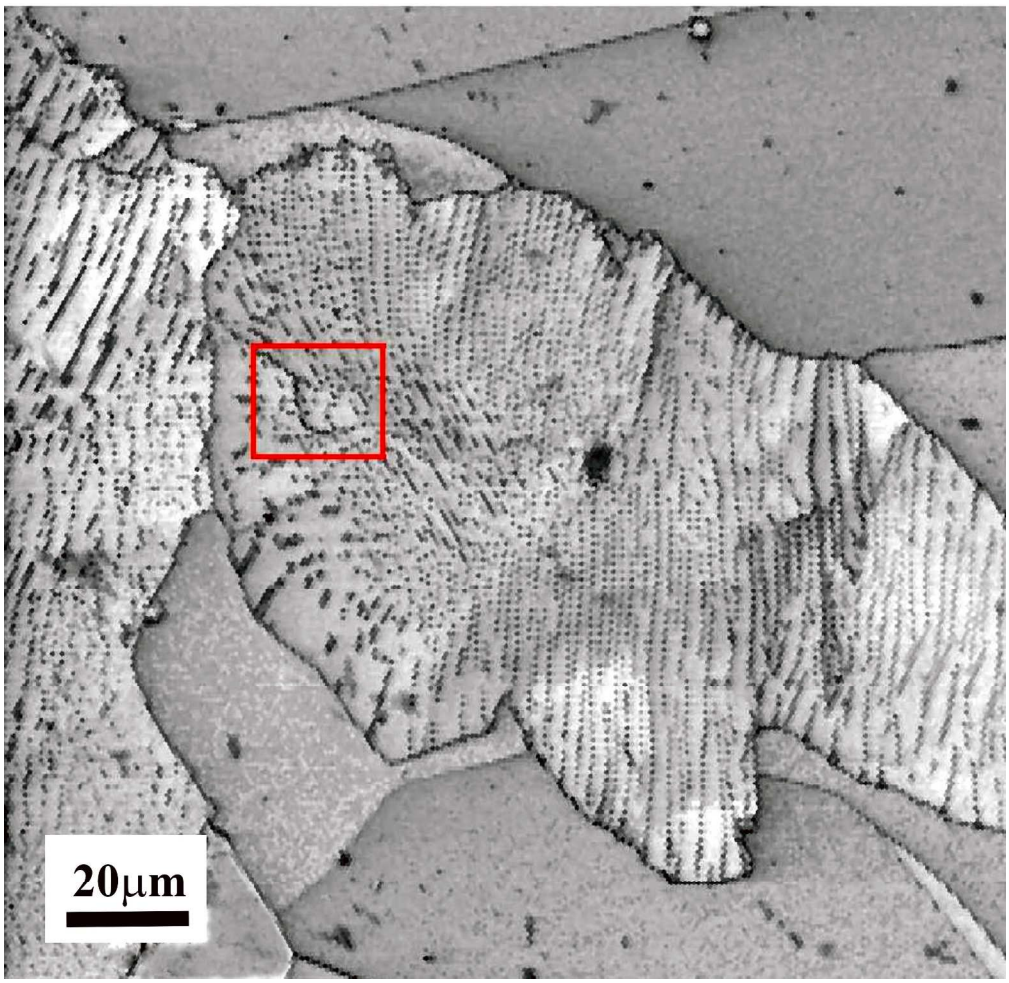

Fig. 11a

233x227mm (300 x 300 DPI)

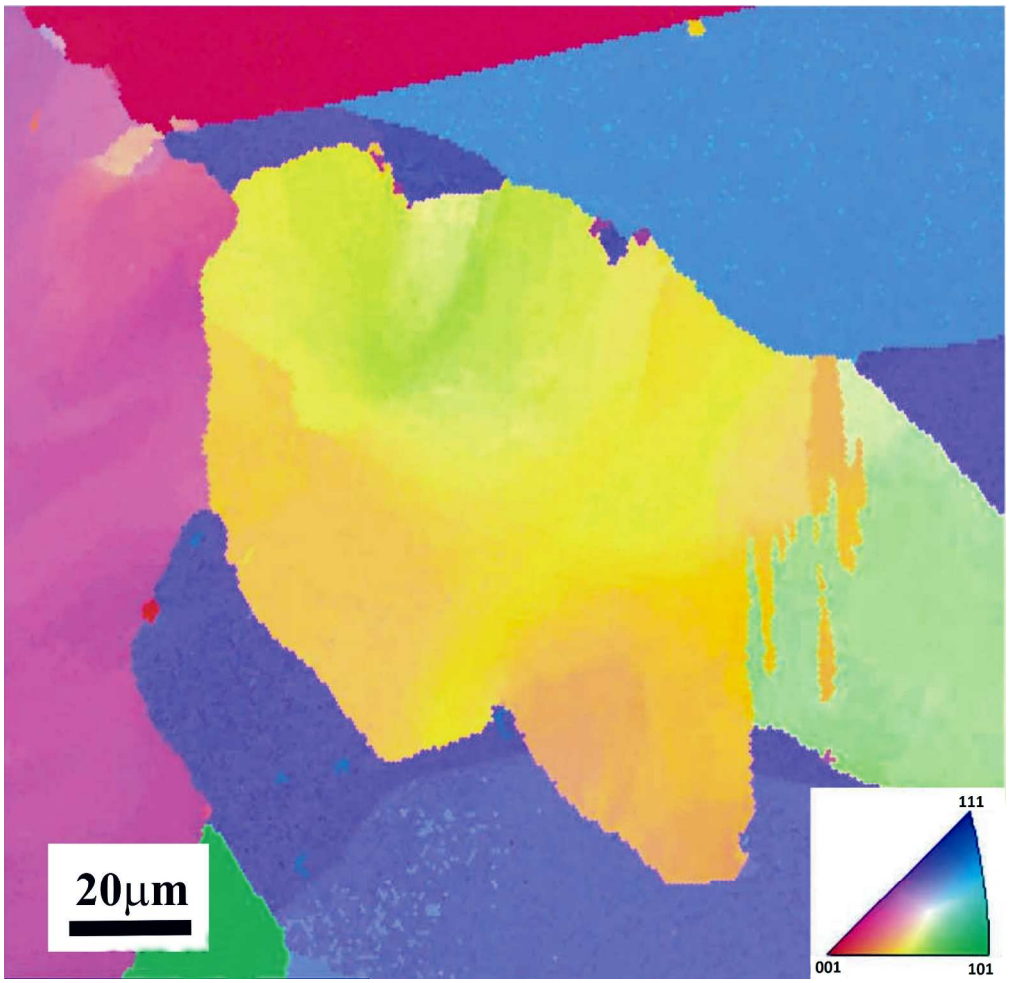

Fig. 11b

732x710mm (96 x 96 DPI)

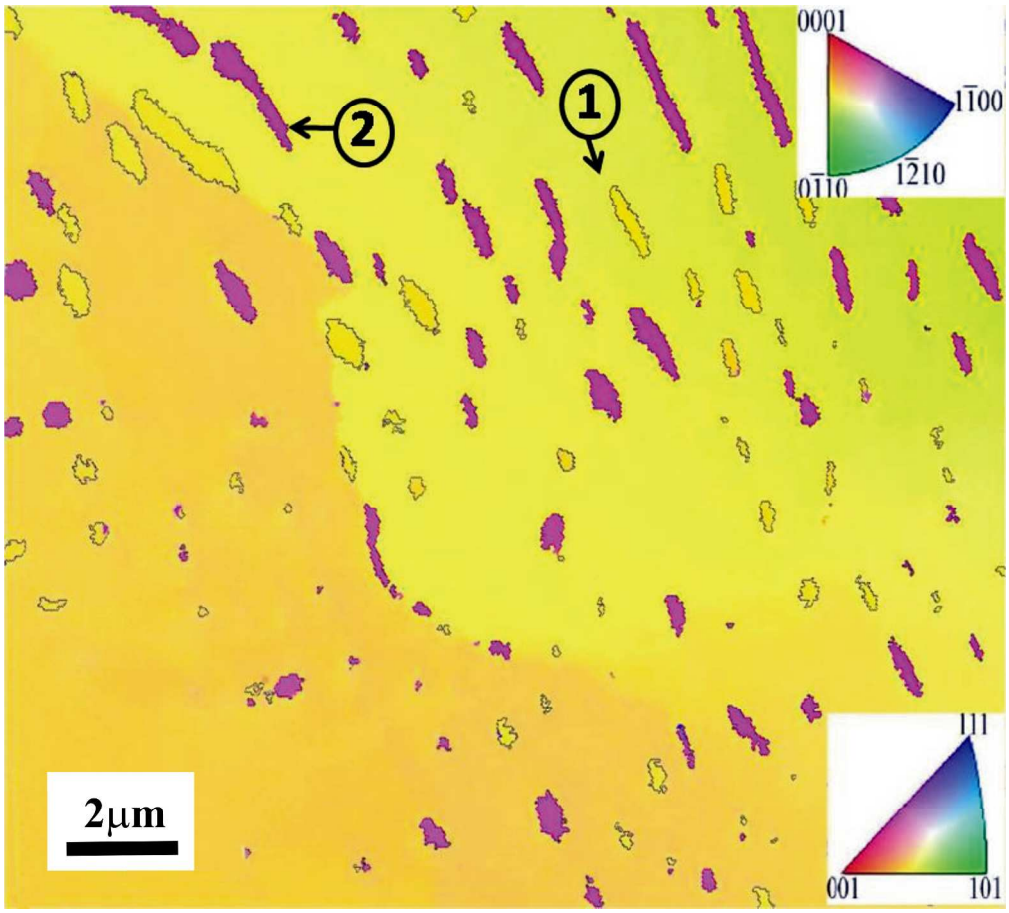

Fig. 11c

801x722mm (96 x 96 DPI)

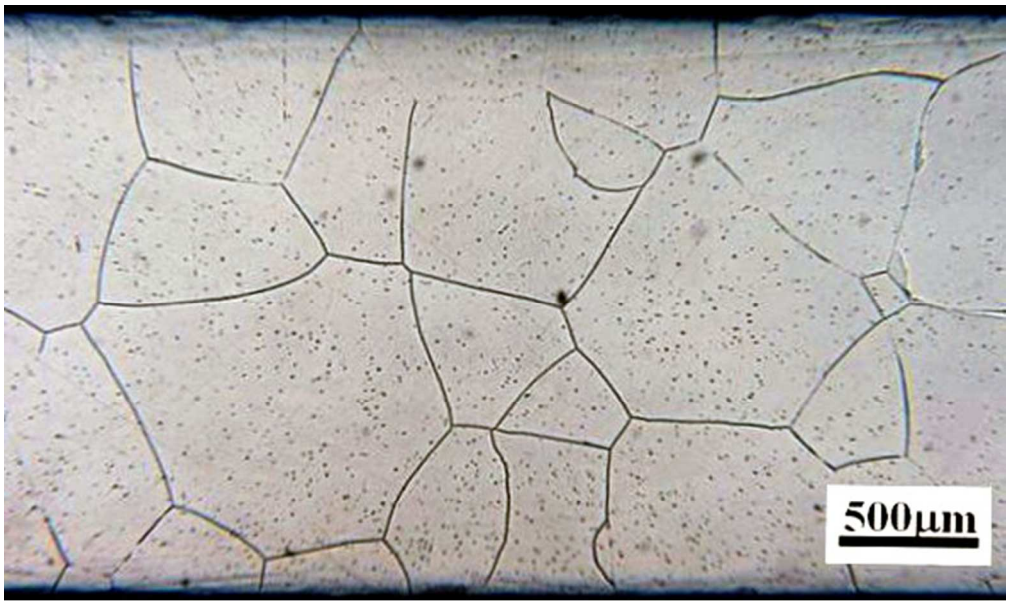

Fig. 12a

156x93mm (96 x 96 DPI)

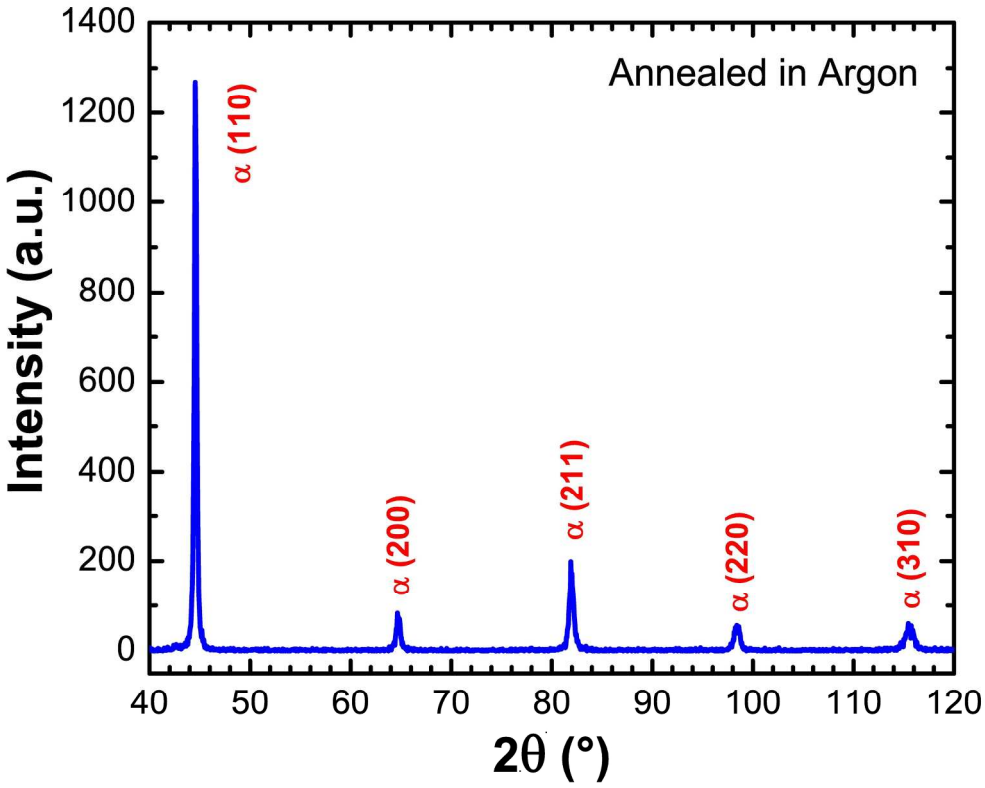

Fig. 12b

214x170mm (300 x 300 DPI)